Preparation and Characterization of Novel Amidated Pectin-Gelatin-Oxidized Tannic Acid Hydrogel Films Supplemented with In-Situ Reduced Silver Nanoparticles for Wound-Dressing Applications

Ilyas Benkhira, Faiza Zermane, Benamar Cheknane, Djalal Trache, Nicolas Brosse, Annalisa Paolone, Henni Chader, Widad Sobhi

Preparation and Characterization of Novel Amidated Pectin-Gelatin-Oxidized Tannic Acid Hydrogel Films Supplemented with In-Situ Reduced Silver Nanoparticles for Wound-Dressing Applications

Ilyas Benkhira [1,*], Faiza Zermane[1], Benamar Cheknane[1], Djalal Trache[2], Nicolas Brosse[3], Annalisa Paolone[4], Henni Chader[5], Widad Sobhi[6].

1. *Laboratoire Chimie Physique Des Interfaces Des Matériaux Appliqués à l'Environnement, Département de Génie Des Procédés, Université Saad Dahlab Blida 1, 09000 Blida, Algeria.*
2. *EMLab, Teaching and Research Unit of Energetic Processes, Polytechnic Military School, BP 17, Bordj El-Bahri, 16046 Algiers, Algeria.*
3. *LERMAB, Faculty of Science and Technology, University of Lorraine, Vandoeuvre-Les-Nancy, 54506, France.*
4. *Istituto dei Sistemi Complessi, Consiglio Nazionale delle Ricerche, Piazzale A. Moro 5, I-00185 Rome, Italia.*
5. *Department of Pharmacy, Faculty of Medicine, University of Algiers 1, Algiers 16001, Algeria.*
6. *Research Center of Biotechnology (CRBt), Constantine 25000 Algeria.*

*Corresponding Author E-mail: ilyesrani27@gmail.com

Abstract

Wound dressings play a pivotal role in shielding injured tissues and facilitating the healing process. However, fabrication of antibacterial wound dressing often entails entail intricate procedures and incorporates toxic constituents. In this study, we developed a novel hydrogel film (AP:GE@OTA/Ag) consisting of amidated pectin (AP), gelatin (GE), oxidized tannic acid (OTA) in different contents (from 0 to 5% wt.%), and in-situ formed silver nanoparticles (AgNPs). Our approach, grounded in an economically feasible method, harnesses the potential of a biocompatible polysaccharide to promoting wound healing. The FTIR and XRD patterns showed that the crosslinking process is the result of interactions between OTA quinone groups and the available free amino groups in AP and GE. SEM images showed homogenous and interconnected structures characterized by sought dispersion of the AgNPs on the surface. Furthermore, TG measurements revealed a good improvement of the AP:GE@OTA/Ag thermal stability compared to the AP:GE film. The fabricated AP:GE@OTA/Ag films exhibited not only improved fluid uptake ability (90.96% at 2h), water retention capacity (91.69% at 2h), water vapor transmission rate (1903.29 $g/m^2/day$), but also demonstrated enhanced tensile strength (38 MPa). Moreover, they displayed cytocompatibility and sustained potent antimicrobial activity against both S. aureus and E. coli at remarkably low AgNPs loadings of 1.02 ± 0.13 $\mu g/cm^2$. Furthermore, NIT-1 mouse insulinoma cells exhibited robust proliferation when cultured with the prepared dressings. These composite structures significantly accelerated wound repair in a skin excision model, suggesting their potential clinical applicability for hemostasis and wound healing.

Keywords: Amidated pectin; wound dressing; oxidized tannic acid; covalent crosslinking; silver nanoparticules.

1. Introduction

Nowadays, the scope of wound dressings has transcended their conventional role of simply protecting wounds. Incorporating diverse functional elements into dressings enhances the wound-healing process and enables monitoring of biological parameters at the wound site [1]. Developing biocompatible and biodegradable films with sufficient physicochemical characteristics, mechanical properties and excellent retention capacity of physiological fluids that are cytocompatible, hemostatic, and own both anti-inflammatory and antimicrobial properties emerged as one of the most promising research areas in this field [2]. Indeed, these multifunctional films allow for accelerating wound healing and simultaneously provide higher protection against bacterial infection with minimal time and cost [3].

Extensive research in the realm of wound dressings has investigated the use of hydrogels, exploring both synthetic polymers and natural polymers either individually or in combinations [4]. In our study, we have specifically focused on natural polymers, namely pectin and gelatin, selected for their remarkable biocompatibility and biodegradability attributes [5, 6].

Blending pectin and gelatin has been extensively explored by the scientific community, particularly in the context of investigating protein-polysaccharide interactions aimed at the development of innovative biomaterials [7]. Recently, photocrosslinked hydrogels were developed by Bostancı et al. [8] by employing methacrylated forms of pectin and gelatin, loaded with varying concentrations of curcumin to serve as stable antibacterial wound dressings.

Osetrov et al. [9] have introduced the potential use of small oxidative agents like DMSO and H_2O_2 to synthesize gelatin-tannin hydrogels. These hydrogels exhibit improved water and oxygen permeability, as well as favorable mechanical properties, rendering them highly suitable for wound dressing applications when compared to KIO_4 and $KMnO_4$. Similarly, Yang et al. [10] have explored the incorporation of both OTA and ferric ions into a gelatin matrix to create composite hydrogels characterized by high mechanical strength, mechanical tunability, a high gelation temperature, rapid self-healing capabilities, and notably low gelation times.

Nevertheless, it is worth noting that bacterial infection remains a significant impediment to wound healing. To the best of our knowledge, the incorporation of OTA and the AgNPs to enhance toughness, increase water resistance, and provide antibacterial properties to AP:GE

hydrogel films through Schiff base reactions and metal coordination remains an unexplored area of study.

Pectin, an anionic heteropolysaccharide abundant in fruits and vegetables, is widely used in pharmaceutical applications such as cancer targeting, wound healing, and drug administration [11]. However, due to their hydrophilic nature, limited thermal stability, and poor mechanical properties, films derived from pectin manifest a predisposition to readily absorb water and undergo disintegration within aqueous environments; hence blending with alternative biopolymers should be performed ahead.

On the other hand, gelatin is a biodegradable protein-based macromolecule that shares chemical similarities with the extracellular matrix of the skin and develops an influential nanofibrous structure for skin regeneration [12]. However, its weak mechanical strength and poor water barrier prevent its biomedical application when it is used alone [13]. For instance, gelatin is often combined with pectin via intermolecular hydrogen bonding and electrostatic interactions, yielding blend films with enhanced hydrophilicity, improved physicomechanical properties, and heightened wound healing capabilities [14-16]. Incorporating cross-linking agents is required to create a compact cross-linking network within the film matrix, thereby ensuring the stability and mechanical resilience of the wound dressing [17].

However, most of the chemical crosslinking agents such as glutaraldehyde, carbodiimides, and polyepoxy compounds are unsuitable for blending gelatin with a natural polymers due to their residues, which may lead to toxic effects and reduce biocompatibility [18]. Thus, there is growing interest in naturally derived cross-linking agents [19]. Tannic acid (TA) emerges as a promising candidate, being a biocompatible, nontoxic, and abundant polyphenolic plant extract. TA exhibits diverse pharmacological properties, including anti-inflammatory and antimicrobial effects, as well as the ability to promote cell proliferation and enhance wound healing through multiple binding sites and interactions [20]. Furthermore, the antioxidant and antitumor attributes of TA have garnered considerable attention in recent decades [21].

Silver nanoparticles (AgNPs) are commonly incorporated in biopolymer-based composite films to tune antibacterial activity [22]. To mitigate undesired aggregation and excessive cytotoxicity associated with direct AgNPs addition recent studies have demonstrated the efficacity of an in-situ reduction method using TA as both a natural reducing and stabilizing agent [23]. This approach enables the preparation of AgNPs with controlled size and improved dispersibility in polymer networks, which can be adjusted according to the degree of crosslinking density [24].

It should be noted that in the current study, straightforward, environmentally safe, and cost-effective green methodologies have been employed for the creation of multifunctional hydrogels based on pectin and gelatin. The basic requirement for the eco-friendly synthesis of AgNPs is silver nitrate in combination with a naturally derived reducing agent.

Therefore, this work aimed to develop and characterize, as a first attempt, antibacterial wound dressings, composed of pectin functionalized with primary amine groups (AP) and GE, supplemented with OTA and AgNPs through a Schiff base reaction and in-situ reduction, respectively. The effect of the mass fraction of the crosslinking agent OTA on the physicochemical, mechanical, thermal, and barrier properties of the prepared films was also investigated using various analytic techniques, e,g, FTIR, XRD, SEM, μXRF, TGA, and tensile strength tests. The hemo-compatibility and in vivo performance of the developed dressings has been compared to that of a commercially available dressing, Hydrocoll®. The cytotoxicity, antibacterial activity, and silver release were also assessed.

2. Experimental and methods

2.1. Materials

Pectin (from citrus) USP with a degree of methoxylation of 65% and galacturonic acid content of 74% was used for the preparation of films (Spectrum chemical, Spain). The gelatin used, in powder form, was of pharmaceutical grade, and bovine origin (Type B, 80-100 Blooms), with a molecular weight of 41.000 g/mol, density = 1358 kg/m^3 and a pH of 4.5 to 5.5 at 25°C (PanReac AppliChem, Spain). Chemicals of analytical grade, namely, tannic acid (TA) (powder form, food grade, VWR International, France), glycerol and sodium azide (NaN_3) (Biochem Chemopharma Co, Canada), silver nitrate ($AgNO_{3)}$ and sodium hydroxide (NaOH) (Merck, Germany), hydrogen peroxide (H_2O_2), 2,4,6-Trinitrobenzene sulfonic acid/TNBS 5% (Sigma-Aldrich, Germany), sodium dodecyl sulfate SDS (Sigma-Aldrich, Germany), the simulated body fluid (SBF) (Biochemazone, Canada), silver standard stock solution (Sigma-aldrich, Germany), and Phosphate-Buffered Saline/PBS (Scharlau, Spain), have been used. Hydrocoll®, a commercial dressing consisting of a wound contact layer of caboxymethylcellulose hydrocolloid particles contained within an outer gas permeable polyurethane film, was procured from Hartmann, France. Furthermore, ultrapure water obtained using an ELGA PURELAB Option-Q water purification system was employed.

2.2. AP synthesis

The experimental protocol reported by Reitsma et al. was carefully followed to synthesize AP [25]. Briefly, commercial pectin (10g) was dissolved with stirring in a pre-cooled mixture of

40 mL ammonia solution (33%) and 60 mL of isopropanol. The reaction occurred in a closed flask immersed in a water bath maintained at 5°C for 24 hours. The pectin solute was collected by filtration using Whatman® Grade 42 filter paper. Subsequently, the collected solute was resuspended in acidic isopropanol (pH 1.5–2.0) and stirred for 10 minutes, followed by another filtration step. To remove the remaining chlorine, the obtained solid was subjected to multiple washes with 70% isopropanol. Finally, the resulting AP was further washed with pure isopropanol, and the purified substance was air-dried to obtain AP powders.

2.3. TA oxidation

The synthesis of oxidized tannic acid (OTA) was carried out following the experimental protocol reported by Osetrov et al. [26]. Briefly, 0.26g of TA was added to 0.6 mole of a hydrogen peroxide solution (3% H_2O_2, pH=10). The pH was adjusted by adding NaOH (2M). The mixture was continuously stirred at 70°C for 30 minutes. Subsequently, the suspension was brought to a neutral pH of 7 using 6M HCl, and the resulting OTA was recovered by filtration process and rinsed with ultrapure water. The obtained OTA was dried at 40°C and kept in desiccators for subsequent use.

2.4. Preparation of the AP:GE@OTA/Ag hydrogel films

A mixture of 5g of GE and AP in a weight ratio of 3:2 was suspended in 100 mL of ultrapure water at 60°C. This ratio of the constituents was chosen following previous investigations [16]. Sodium azide was added at a concentration of 0.02% as an antimicrobial agent to prevent fungal contamination. Continuous stirring was maintained until the complete dissolution of the biopolymers was achieved. Subsequently, an OTA solution at different concentrations (0%, 0.5%, 1%, 2%, and 5% based on the total weight of the AP and GE, respectively) was added dropwise over the polymer blend under stirring at 60°C for 30 minutes to facilitate the cross-linking. After, glycerol was added as a plasticizer to each crosslinked blend at 40% w/w of the total dry biopolymer weight and stirred continuously for 16 hours at 60°C to obtain a homogeneous solution. The plasticized dispersions were then degassed and cast by pouring onto Petri dishes (90 mm diameter) in quantities of approximately 20g. The cast films were allowed to dry in an open-air environment at room temperature for 3 days.

After drying, the films were peeled off their supports and immersed in a solution of silver nitrate (20 mg/L, pH of 7.6) for 30 minutes [27]. Subsequently, the films were subjected to

multiple washes using ultrapure water, air-dried, and conditioned in desiccators at a relative humidity of 53% and a temperature of 25°C for 7 days prior to testing.

In the upcoming section, the resulting biopolymer films with different OTA concentrations, are labeled as follows: AP:GE, AP:GE@OTA0.5%/Ag, AP:GE@OTA1%/Ag, AP:GE@OTA2%/Ag and AP:GE@OTA5%/Ag.

2.5 Characterization

2.5.1 Determination of degree of amidation (DA)

The degree of amidation was obtained by deconvolution of FTIR spectra (1800–1500 cm^{-1} of AP). This analysis was carried out using Origin software. The DA was calculated as the ratio of the area of the band at 1667 cm^{-1} (A_{amide}) on the sum of areas of free, methyl-esterified and amidated galacturonic acids (A_{tot}) at 1724, 1584 and 1667 cm^{-1}, respectively, according to the following equation [28] :

$$DA\ (\%) = \frac{A_{amide}}{A_{tot}} \times 100 \qquad (1)$$

2.5.2 Determination of the amine content and the degree of crosslinking

The quantification of uncrosslinked primary amino groups ($–NH_2$) in AP and GE matrices was performed using a UV assay with TNBS [29]. Crosslinking extent was assessed by the difference in chemically determined free primary amine groups before and after crosslinking [30]. Each sample with a mass of 11mg was mixed with a freshly prepared TNBS solution (1 mL of 0.5% w/v TNBS, 1 mL of 4% w/v $NaHCO_3$). After a 4 h incubation at 40°C, 3 mL of 6N HCl were added, followed by autoclaving (120°C, 1 h). The resulting solution was diluted with ultrapure water (5 mL), extracted with 8 mL of ethyl ether to eliminate excess unreacted TNBS. Finally, a 5 mL aliquot from each sample was heated in a hot water bath for 15 min to evaporate residual ethyl ether, then diluted with 15 mL of ultrapure water. Absorbance at 346 nm was measured with a Shimadzu model UV-1900i spectrophotometer against blank samples prepared using the same procedure, except HCl was added before TNBS to prevent any reaction between TNBS and biopolymers. Free primary amino groups per gram of material (Nε) in non-crosslinked and crosslinked samples were calculated using Equation (2).

$$\mathrm{N}\varepsilon = \frac{Mol\ of\ \varepsilon{-}amino}{g\ of\ material} = \frac{2(absorbance)(V)}{\left(1.46 \times 10^4 \frac{L}{mol.cm}\right).b\ .x} \qquad (2)$$

Where the molar absorptivity coefficient of the formed colorimetric complex (TNP-lys) is represented as 1.46×10^4 L/mol.cm, with V = 0.02 L indicating the volume of the water solution containing hydrolyzed samples post- ether evaporation. The variables b = 1 cm

denote the cell path length, and "x" corresponds to the sample weight (g). The crosslinking degree (f) was subsequently deduced according to Equation (3).

$$f\,(\%) = \left(1 - \frac{\text{Absorbance of crosslinked sample}}{\text{Absorbance of uncrosslinked sample}}\right) \times 100 \qquad (3)$$

Each determination was conducted in triplicate. The non-crosslinked samples were considered to contain 100% of the initially available free amine groups, serving as a reference for estimating the percentage of remaining free amine groups after the crosslinking reaction.

2.5.3 Structural, morphological, thermal, and mechanical properties

The structural analysis of the AP:GE@OTA/Ag hydrogel films was conducted using various analytical techniques. The FTIR spectra of the AP:GE@OTA and AP:GE@OTA/Ag films were recorded in ATR mode using an Alpha II FTIR spectrometer (Bruker, Germany). The measurements were performed between 400 to 4000 cm^{-1} by adding 32 scans with a resolution of 1 cm^{-1}. The ^{1}H-NMR spectra of PE and AP were recorded in Deuterium Oxide (D_2O) solution using an NMR spectrophotometer (Ascend 400 MHz, Bruker, Switzerland).

The morphologies and distribution patterns of metal ions within the films were observed by scanning electron microscope-energy dispersive spectrometry (SEM-EDS, FEI Inspect-S50, Czech Republic). Additionally, X-ray diffraction (XRD) patterns of PE, AP, and both the AP:GE@OTA and AP:GE@OTA/Ag films were recorded on a SmartLab X-ray diffractometer (Rigaku Corp., Japan), scanning from $2\Theta = 5°$ to 80° with steps of 0.01°. The chemical composition of the hydrogel films was determined using a micro-X-ray fluorescence spectrometer (μXRF, XGT-9000 Pro, Horiba-Jobin-Yvon) working for elements between F and Am. Based on these spectra, 2D elemental maps of the specimens were generated, with each distinct color and its relative intensity representing a specific element and its content. A background color signifies the absence of an element or the presence of hollow regions. To assess the thermal behavior, thermogravimetry (TG) experiments were conducted using a Q600 SDT instrument (TA Instruments, USA) at a heating rate of 10°C.min^{-1} and under a nitrogen atmosphere.

The film thickness parameter was determined using a Mitutoyo micrometer (Tokyo, Japan), and the measurements were performed at five random locations on each hydrogel film, and the average thickness values of the films were computed.

The tensile properties of the AP:GE@OTA/Ag films were evaluated through the determination of the tensile strength (TS), elongation at break (EB), and Young's modulus

(YM) using a universal tensile machine (MTS Criterion universal testing machine, model 45, USA) in accordance with the ASTMD-882-88 standard test method [31]. Samples were prepared as pieces measuring 25.4 × 150 mm (width × length). The experiments were carried out with a gauge length of 50 mm and a crosshead speed of 50 mm/min. Five tests were performed to evaluate the average tensile strength, the percentage of elongation at break, as well as Young's modulus based on the stress−strain curves.

2.5.4 Fluid absorption ability, water storage capacity, and water vapor transmission rate

The determination of the fluid absorption capacity of dried AP:GE@OTA/Ag films was evaluated gravimetrically in triplicate with an accuracy of ± 5% [32]. Beforehand, the samples were subjected to a drying process until they reached an invariant weight. The samples were then precisely cut into strips of uniform dimensions (30 x 30) mm^2, weighed, and submerged in vials filled with 15 mL of PBS solution (pH 7.4) at a temperature of 37°C. At each predefined time interval, the strips were carefully removed from the vials and the extra amount of PBS solution present on the surface was softly blotted with a filter paper. The swollen samples were then reweighed to determine the weight change. This process was repeated multiple times until no further alteration in weight was observed. The swelling equilibrium (%) was then calculated using Equation (4):

$$\text{Equilibrium of fluid content } (\%) = \left(\frac{W_t - W_0}{W_0}\right) \times 100 \qquad (4)$$

where W_t is the weight of the swollen and W_0 stands for the weight of the dry film.

For the assessment of the water retention capacity, each film was immersed in ultrapure water for 24 hours. The samples were removed from water and the remaining extra amount of water on the surface was softly removed by blotting with a filter paper. The wet films were then weighed (W_0) and kept in an open-air environment (T= 25°C, RH= 75%) for specific time intervals (W_t). The water storage ratio was determined in triplicate according to Equation (5):

$$\text{Water storage capacity } (\%) = \left(\frac{W_t}{W_0}\right) \times 100 \qquad (5)$$

The measurement of the water vapor transmission rate (WVTR) was performed gravimetrically in triplicate, following ASTM standard method [33]. Briefly, 10 mL of distilled water was poured into a cylindrical glass vial with a diameter of 34 mm. The vial's opening was then completely sealed with a test specimen, firmly affixed using Teflon tape along the edges to prevent any water vapor leakage through the borders. Subsequently, the vials were placed inside an incubator (T=37°C, RH= 35%) for 48 hours. The evaporation-

induced loss of water through the sample was periodically measured by weighing. By analyzing the weight loss versus time plot, the WVTR of each tested specimen (in g/m^2/day) was calculated according to Equation (6):

$$\text{WVTR}\ (g/m^2\ /\text{day}) = (slope \times 24)/A \quad (6)$$

where A (mm^2) denotes the permeation area of the film.

2.6 Biological characterization

2.6.1. Antibacterial activity test

To reveal the infection-resistant efficacy of both AP:GE@OTA and AP:GE@OTA/Ag formulations in comparison to the AP:GE film, an inhibition zone method was employed against Staphylococcus aureus (S. aureus, ATCC 6538, gram-positive bacteria) and Escherichia coli (E. coli, ATCC 8739, gram-negative bacteria). Briefly, each film was cut into 6 mm diameter discs and underwent sterilization under a UV lamp for 30 min before being placed on the freshly prepared LB agar plates, where 100 μL of a bacteria suspension (10^8 CFU/ml) was uniformly spread over the surface. Following incubation at 37°C for 24 h, the diameter of the resulting inhibition zone around each sample was measured from ImageJ software with digital images of plates [34]. The experiment was conducted in triplicate within a biosafety cabinet.

2.6.2. Hemocompatibility test.

Hemolysis and anticoagulant assays were performed to evaluate the hemocompatibility of the prepared dressings. In the hemolysis assay, human red blood cells (HRBCs) were acquired by eliminating serum through centrifugation, followed by five washes with PBS, as previously described [35]. Afterward, the HRBCs were appropriately diluted tenfold with PBS. Subsequently, 2 mL of the diluted HRBCs suspension was dispensed into separate 5 mL sample vials, each containing 1mg of the corresponding dressings, namely AP:GE, AP:GE@OTA0.5%, AP:GE@OTA5%, and AP:GE@OTA0.5%/Ag, AP:GE@OTA5%/Ag. As controls, two additional sample vials were used: one with 0.4 mL of diluted HRBCs and 1.6 mL of water (positive control), and other with 1.6 mL of PBS solution (negative control). After incubation at 37°C for 2 h, the above mixtures underwent centrifugation at 10,000 rpm for 1 minute and the absorbance (A) of the resulting supernatants was measured at 541 nm using a Shimadzu model UV-1900i spectrophotometer. The hemolytic percentage (HP) was then calculated as follows [35],

$$HP\ (\%) = \frac{(A_{sample} - A_{negative\ control})}{(A_{positive\ control} - A_{negative\ control})} \times 100 \quad (7)$$

The blood coagulation index (BCI) was assessed by the kinetic clotting time method, following the procedures outlined by Wang et al. [36]. Initially, the prepared films and Hydrocoll® commercial wound dressing were cut into disk-shaped specimens (6 mm diameter) and sterilized under UV light for 1 h, followed by triple rinsing with PBS. These samples were then placed in flat beakers, onto which 0.25 mL droplets of freshly collected ACD human blood were dispensed, followed by the addition of 0.02 mL of $CaCl_2$. After incubation at 37°C for 10, 20, 30, and 50 min, 50 mL of distilled water was sequentially added at each time point. Following an additional 5-min incubation, hemolyzed blood was collected and measured spectrophotometrically at 542 nm. Each experimental group was conducted in triplicate. The BCI was calculated using the following formula:

$$\text{BCI}\ (\%) = \left(\frac{\text{Absorbance of blood which had been in contact with sample}}{\text{Absorbance of solution of distilled water and ACD blood}}\right) \times 100 \quad (8)$$

2.6.3 In vitro silver release behavior

The evaluation of in vitro silver release through AP:GE@OTA/Ag films was conducted using a Franz vertical diffusion cell with eggshell membranes positioned between the donor and receptor compartments, following the methodology as described by Gupta et al. [37]. The membranes were pre-equilibrated by immersion in SBF for 24 h. AP:GE@OTA/Ag dressings (1 cm^2 each) were placed over the membranes in the donor compartment, ensuring continuous contact with the receptor compartment filled with 30 mL of pH 7.4 SBF. The assembly was maintained at 37°C with stirring at 50 rpm. At specific intervals over a 48-hour period, 3 ml aliquots were collected and replaced with an equal volume of SBF to maintain the receptor phase at 30 ml. Silver content in each aliquot was analyzed using a graphite furnace atomic absorption spectrometer (GFAAS) (AA7000, Shimazdu, Japan) at 328.1 nm. Calibration standards (0.5 ppm to 5 ppm) were prepared from a 1000 ppm silver standard stock solution for generating a calibration curve. Cumulative silver permeation per square centimeter of dressings was plotted against incubation time. To determine overall silver loading, 20mg of each AP:GE@OTA/Ag formulation was digested in 30 mL of 70% nitric acid, and a 3 mL sample was analyzed using GFAAS. Each experiment was replicated three times.

2.6.4 Cytotoxicity test using XTT bioassay

2.6.4.1 Cell culture conditions

The NIT-1 mouse insulinoma cell line (CRL-2055) were obtained from the American Type Culture Collection (ATCC) in Washington, DC, USA. These cell lines were cultured using RPMI-1640 medium, enriched with 10% fetal bovine serum (FBS) and 1% penicillin/streptomycin. The culturing process was carried out in an incubator set to a 5% CO_2

atmosphere at a constant temperature of 37°C. A traditional trypan blue staining method was employed alongside the Neubauer counting chamber for cell quantification, allowing for accurate cell viability assessment and counting.

2.6.4.2 Cytotoxicity assay

NIT-1 mouse insulinoma cells (CRL-2055) were used to assess cytotoxicity of the prepared dressings using XTT assay [38], employing XTT cell proliferation kit sourced from Roche Company (Bale, Switzerland). The NIT-1 cells were seeded into a 96-well microplate and incubated at 37°C in a 5% CO_2 atmosphere for 24 h for cell attachment and growth. Each sterilized dressing (6 mm diameter) was dissolved in PBS, and dilutions ranging from 100 µg/ml to 12.5 µg/ml were prepared. After the initial 24-hour incubation period, the samples were added to experimental wells in triplicate at varying concentrations. Subsequently, cells were further incubated for 72 h. Post-incubation, the XTT reagent was applied to the cells, and cell viability was assessed by comparing their absorbance with those of the PBS at 490 and 660 nm using a microplate reader. Cell viability was calculated by using the following equation [39] :

$$\text{Cell Viability (\%)} = \frac{\text{Absorbance of Sample}}{\text{Absorbance of control group}} \times 100 \qquad (9)$$

2.6.5 In vivo wound healing studies

Full-thickness surgical excisions were performed to assess the wound healing-promoting capabilities of the hydrogel films. The animal procedures were conducted in accordance with the guidelines of the Algerian Association for Animals Experimentation Science, as approved under permission number XXXX, dated X X, 20XX.Twenty-one Wistar albino rats (male, age 6 months, 200±20g) from the animal household of the pharmacotoxicology department of the National Pharmaceutical Products Control Laboratory (NPPCL) were randomly divided into four groups, each comprising seven rats. The group allocations were as follows:

Group I: Control (Wound + Hydrocoll®)

Group II: Wound + AP:GE dressings

Group III: Wound + AP:GE@OTA5% dressings

Group IV: Wound + AP:GE@OTA0.5%/Ag dressings

The rats were individually housed in hygienic conditions for several days before the study to acclimatize to the laboratory environment (22 ± 2°C, RH of 50%). They were provided with standard rodent feed and water ad libitum throughout the study, while maintaining a 12 h

light/dark cycle. Before surgery, anesthesia was induced via intraperitoneal injection of Thiopental at a dosage of 45mg/kg body weight. Dorsal hairs were shaved, and the skin was sterilized with 70% ethanol. Using a surgical blade and forceps, full-thickness round wounds measuring 3 mm in diameter were created on the cervicodorsal area under strict aseptic conditions. Excess blood was absorbed using sterile surgical compresses, and wound margins were cleaned with surgical alcohol. Postoperatively, rats received a single intravenous injection of 10mg of paracetamol to alleviate pain, adhering strictly to guidelines for the Care and Use of Laboratory Animals, given the susceptibility of rodents to self-mutilation in response to severe pain. Subsequently, the wounds were covered with freshly prepared AP:GE, AP:GE@OTA5% and AP:GE@OTA0.5%/Ag dressings, while the positive control group received Hydrocoll®. Dressings were changed daily. Wound healing progression was monitored and documented via digital photography on the 2nd, 4th, 6th, 8th, 10th and 12th postoperative days. Throughout this period, rats were handled gently to minimize stress and acclimate them to the laboratory environment. The repair area was calculated using Image J software, and the wound contraction was determined by the following equation :

$$\text{Wound contraction}(\%) = \frac{initial\ wound\ area - wound\ area\ at\ D_x}{initial\ wound\ area} \times 100 \qquad (10)$$

2.7 Statistical Analysis

The experimental results were statistically analyzed using SPSS statistics V26 software (IBM Corp., Armonk, NY, USA) employing a one-way analysis of variance (ANOVA) and a confidence level of 95%. To identify significant differences among the groups, Tukey's test was performed, and a p-value <0.05 was considered indicative of statistical significance.

3. Results and discussion

3.1. AP characterization

Commercial pectin (PE) was chemically modified before the film preparation by an amide reaction leading to AP. Figure 1(a) displays the FTIR spectra of both types of pectin, i.e., the non-amidated and amidated ones. In the pectin spectrum, the peak at 3370 cm^{-1} is attributed to the stretching vibration of -OH groups. The peak at 2932 cm^{-1} corresponds to the C–H stretching vibration, while the peak at 1724 cm^{-1} indicates the stretching vibration of the methyl ester. The peaks at 1436 cm^{-1} and 1340 cm^{-1} can be assigned to $–CH_2$ scissor and –OH bending vibrations, respectively [40].

Furthermore, the sharp peak spotted at 1006 cm^{-1} is assigned to the glycosidic bonds that connect two galacturonic sugar units [41]. The FTIR spectrum of AP showed a broadening

accompanied by a significant increase of the peak at 3370 cm^{-1}, which is attributed to the amide N-H peak and the strong broad O-H [42]. Additionally, the peaks observed at 1667 cm^{-1} (amide I) and 1584 cm^{-1} (amide II) were the result of the electron doping from $–NH_2$, which is in agreement with the reported amide band FTIR peak at 1590 cm^{-1} [28]. The AP spectrum displayed also a weak peak at around 1423 cm^{-1}, suggesting that the amide group was successfully incorporated into the pectin molecules. The DA of AP obtained by deconvolution FTIR spectra was 38.62±0.04%.

Figure 1(b) shows the X-ray diffractograms of PE and AP. The obtained pattern obtained for the unmodified pectin exhibits well-defined peaks at 2θ angles of 9°, 18.54°, 28.44°, and 40.21°, indicating its semi-crystalline nature. In contrast, the pattern of AP shows two weak and broad diffraction peaks at around 13.34° and 20° (2θ). The incorporation of the $–NH_2$ groups could have obstructed the rearrangement of pectin molecular chains, causing the disruption of its crystalline structure.

Figure 2 displays the ^{1}H-NMR spectra of PE and AP. The NMR spectrum of AP showed prominent peaks within the 3-5.5 ppm range, these chemical shifts correspond to hydrogen atoms on the polygalacturonic acid chain of pectin [43]. Furthermore, the strong peak in the range of 3-4 ppm were assigned to the methyl protons on the nitrogen of primary amine inserted in the PE chains. This suggests the partial methylation of the methoxy groups in the pectin molecules [42], indicating the successful preparation of AP.

The results provided by the spectroscopy techniques (FTIR, XRD, and ^{1}H-NMR) allow concluding that the PE was successfully functionalized with primary amine groups according to the reaction presented in Figure 3, leading finally to AP.

3.2. AP:GE@OTA/Ag film characterization

AP:GE@OTA films were initially created through covalent cross-linking of amino groups in both AP and GE with the carbonyl reactive sites of OTA. Subsequently, under alkaline conditions, OTA phenolic hydroxyls acted as a natural reducing agent for silver ions, leading to the formation of AgNPs. Meanwhile, the existing carbonyl groups on OTA could form coordinate bonds with AgNPs, creating a protective layer that delayed the release of Ag^+ and prevented direct contact between AgNPs and cells [27]. The obtained films are shown in Figure 4 and their formation mechanisms are detailed in the scheme reported in Figure 5. The TNBS reaction has been used for the specific measurement of amino groups in proteins, foodstuffs and peptides [44]. The degree of crosslinking was subsequently calculated as the difference between the chemically determined amount of free amino groups before and after crosslinking. It is presumed that each lost amino group contributes to the formation of a single

crosslink. The data in Table 1 represent the values of free amine groups per gram of material, before and after the crosslinking process, along with the extent of crosslinking in the prepared films. The number of free amine groups in GE was comparable to previous studies [30, 45], and higher than that in AP samples ($31.8 \pm 1.35\times10^{-5}$ mol.g^{-1} compared to $8.5 \pm 0.75\times10^{-5}$ mol.g^{-1}). After the crosslinking process, a significant reduction in the number of free amino groups occurred in the AP and GE matrices, confirming the active involvement of amino groups as highly nucleophilic agents in the film crosslinking. Additionally, Figure 6 demonstrates the impact of OTA content on the crosslinking process concerning amino consumption and the degree of crosslinking. An increase in OTA content correlated with elevated amino consumption. The number of free amine groups in all AP:GE@OTA films decreased after crosslinking within the range of $7.1–29.2\times10^{-5}$ mol.g^{-1}. As a result, the extent of crosslinking exhibited an increase, reaching 58.52±2.68% for AP:GE@OTA2% and 78.27±4.47% for AP:GE@OTA5%, respectively.

3.2.1 Fourier Transform Infrared Spectroscopy (FTIR) measurements

Figure 7(a) displays the FTIR spectra of both TA and OTA. In the case of TA, peaks were observed in the 3200-3700 cm^{-1} range, and around 1316 cm^{-1}, which were assigned to the stretching vibration of the phenolic hydroxyl groups. Peaks at 1192 cm^{-1} and 1536 cm^{-1} were associated, respectively, with the stretching vibrations of the C=O and C=C bonds in the aromatic ring. Additionally, the peak at 1023 cm^{-1} was associated with the ether bonds (C−O−C) stretching vibration. Hydrogen peroxide has the capacity to oxidize phenolic compounds, leading to their conversion into reactive quinones that may react with GE and AP [9]. Moreover, the OTA spectrum highlighted a distinctive peak that emerged at 1626 cm^{-1}, indicating carbonyl stretching vibrations, which may be explained by the formation of an intermediate quinone [10].

The FTIR analysis was conducted to confirm the crosslinking of the blended hydrogel films and to investigate the molecular structures of the AP:GE@OTA and AP:GE@OTA/Ag blends. For a comparative study, the spectra of AP, GE, and OTA were also recorded. From Figure 7(b), it is evident that the GE samples exhibited distinct transmittance peaks in the frequency range of 3320 cm^{-1}-3520 cm^{-1} due to the establishment of hydrogen bonds between water and amide-A. Furthermore, peaks at 1630 cm^{-1} (amide-I), 1330 cm^{-1} (amide II), 1235 cm^{-1} (amide-III), and a series of peaks spanning from 1460 cm^{-1} to 1380 cm^{-1} were attributed to the symmetric and asymmetric bending vibrations of methyl groups [46].

The FTIR spectrum of AP:GE films displayed transmittance peaks in the range 3200 cm^{-1}-3400 cm^{-1}, representing the stretching vibrations of NH and OH groups, indicative of hydrogen bonding between these functional groups and water molecules [47]. The C=O stretching (amide I) absorption at 1637 cm^{-1} and N–H bending (amide II) bands at 1553 cm^{-1} are representatives of the AP and GE structures. The IR spectrum of AP:GE films suggests a possible physical interaction between the positively charged GE-NH_3^+ derived from gelatin and the negatively charged pectin-COO^-. The C-N stretching vibration peak at 1553 cm^{-1} is significantly stronger in the AP:GE@OTA5% sample compared to that in the AP:GE film. The characteristic peaks in the AP:GE@OTA5% are significantly stronger than those in the AP:GE film, indicating the establishment of new C–N bonds formed through the Michael addition reaction [48]. At the same time, stretching vibration of the carbonyl group spotted at 1630 cm^{-1} was shifted to 1648 cm^{-1} after crosslinking, thus confirm the formation of the imine bond (-C=N) imine bond during Schiff reactions [10]. Furthermore, the presence of –CH stretching vibration peaks in the crosslinked films is indicated by the peaks spotted at 2940 cm^{-1} to 2960 cm^{-1} [49]. The transmission peak observed at 1238 cm^{-1} is attributed to the stretching vibrations of C-O bonds. As shown in Figure 7(c), a decrease in the intensity of the –OH stretching vibration peak in the FTIR spectra of AP:GE@OTA/Ag hydrogel films is recorded compared to the AP:GE@OTA films. This can be attributed to the increase in hydrogen bonding or stronger intermolecular interactions among OTA, AP, and GE within the hydrogel structure.

3.2.2 X-ray diffraction (XRD) analysis

Figure 8(a) shows the X-ray diffractograms for AP:GE, AP:GE@OTA films, and for neat GE. GE exhibited a single diffraction peak within the 2θ range of 15–25°, which aligns with the typical XRD profile of pure gelatin, stemming from the α-helix and triple-helical structure from the collagen renaturation process [50]. The X-ray diffractograms of AP:GE samples revealed broad and diffused peaks at 2θ equal to 15.91° and 38.19°, indicative of the amorphous nature of the blend film. The disappearance of X-ray diffraction peaks corresponding to AP confirms the intermolecular interactions between these two biopolymers, which is in agreement with the results of the work of Mishra et al. [51].

The X-ray diffractograms of AP:GE@OTA formulations exhibited differences compared to those observed in the AP:GE films. When the OTA mass fraction increased, the intensity of the crystal peak of gelatin at 8.10° (2θ) decreased in intensity, while new peaks at 2θ values of 22.95, 21.48, 21.35 and 21.07° appeared for AP:GE@OTA0.5%, AP:GE@OTA1%,

AP:GE@OTA2%, and AP:GE@OTA5%, respectively. These findings suggest that the characteristic helical structure of GE was modified by AP chains during the crosslinking process with OTA. This modification was achieved by disrupting hydrogen bonds and hydrophobic interactions while also creating new Schiff base (–C=N) connections because of the condensation of amine groups in both GE and AP with the carbonyl group present in OTA. These findings highly corroborate the FTIR results discussed previously. Additionally, the first diffraction peak of gelatin at 8°, which is related to the diameter and rate of the triple helix [52], is often reduced in intensity by the addition of polyols such as tannin [53], and glycerol [53].

On the other hand, the XRD patterns of the AP:GE@OTA/Ag samples, shown in Figure 8(b), revealed four prominent peaks ranging from 30° to 80°. To ascertain the precise nature of the silver nanoparticles formed in our experiments, a comparative analysis of the obtained diffractograms with those of pristine crystalline silver structures, as cataloged by the Joint Committee on Powder Diffraction Standards (reference file nos. 04-0783) was conducted. The result clearly confirmed the formation of silver nanoparticles with the face-centered cubic (fcc) structure [54]. This confirmation was derived from the observed peaks at angles of 38.72°, 43.96°, 64.29°, and 77.40°, corresponding to the (111), (200), (220), and (311) crystallographic planes of silver, respectively.

The determination of the nanoparticle size was achieved through the utilization of the full width at half maximum (FWHM) values observed for these reflection planes in conjunction with the Debye–Scherrer equation. The calculated particle sizes derived from the XRD line broadening analysis were in concordance with those ascertained through scanning electron microscopy (SEM) analysis (Table 2). Consequently, these results establish an average particle size of approximately 56 nm.

3.2.3 Scanning electron microscopy (SEM) Analysis

The SEM image obtained for the AP:GE film conjointly with those obtained for all the AP:GE@ OTA films are shown in panel (a) of Figure 9. It is obvious that all the investigated films exhibited translucent, smooth, and homogenous surfaces, indicating that the addition of OTA and AgNPs causes the formation of a compact network structure within AP:GE@OTA/Ag films (see Figure 9(a)). There were no visible pores or cracks on the surface. It is not possible to detect a significant difference in the films produced with different concentrations of OTA. Moreover, a well-dispersed AgNPs had been achieved for the film treated with 2% and 5%. The size of the AgNPs was confirmed by SEM analysis and was found around 57 nm.

EDS analysis was also carried out on the AP:GE@OTA5%/Ag film and the obtained results were illustrated in plot (b) of Figure 9. A distinct peak in the silver region could be easily observed, thus confirming AgNPs formation. The uniform dispersion of AgNPs within the films further highlights the successfulness of the cross-linking process.

3.2.4 Micro X-ray fluorescence (μXRF) analysis

Table 3 presents the relative abundance of elements present in the AP:GE@OTA/Ag hydrogel films, as determined by the μXRF analysis, at the level of impurities. The obtained results confirmed the effective incorporation as well as the homogeneous distribution of the AgNPs over the films for all the investigated samples (Figure 10). These findings strongly corroborate those from the SEM-EDS and XRD analyses. Results revealed that sulfur (S), calcium (Ca), and copper (Cu) are the main elements forming the AP:GE@OTA/Ag hydrogel films. Exception is made for the AP:GE@OTA5%/Ag film, in which, the relative abundance of S, Ca and Ag has been respectively found to be 75.31%, 24.54% and 0.14%.

3.2.5 Mechanical properties of hydrogel films

The tensile testing offers insights into the film's strength and flexibility, as evidenced by its tensile strength and elongation at break. For wound dressing application, it is suggested that films should preferably exhibit both strength and flexibility. This is necessary to ensure durability and enough stress-resistant to meet the requirements for application, handling, and storage. Hence, glycerol, a commonly employed component in hydrogel formulations, was added as a plasticizer (40% w/w of the total dry biopolymer weight) to each crosslinked blend to enhance the flexibility of the film. Table 4 summarizes the mechanical properties obtained for the studied hydrogel, namely, the thickness, the tensile strength, the elongation at break, and Young's modulus.

The thickness parameter was measured using a thickness gauge. The results showed that the thickness ranged from 0.27 mm to 0.41 mm. The uncertainty associated with the thickness is found to be less than 0.08 mm. Furthermore, it was found that the thickness, the tensile strength, and Young's modulus increased with the incorporation of OTA as well as the increase in its mass fraction. Nevertheless, the elongation at break (%) evolution showed an opposite trend.

Results showed (Table 4) that AP:GE@OTA0.5%/Ag film exhibited a significantly higher percentage of elongation (37.73%) and lower tensile strength (23.11 MPa) and Young's modulus (1218 MPa) than those of AP:GE@OTA1%/Ag, AP:GE@OTA2%/Ag and AP:GE@OTA5%/Ag ($p < 0.05$). This result suggested that the addition of 0.5 wt.% OTA was enough to generate a flexible AP:GE@OTA/Ag hydrogel film, by improving its mechanical

properties. The highest mass fraction used of OTA (5%) confers to the film the highest toughness and rigidity. This may be well appreciated through the high values of tensile strength (38.49 MPa) and Young's modulus (1512.98 MPa), along with a low value of elongation at break (32.42%) ($p < 0.05$). The AP:GE@OTA2%/Ag films demonstrated slightly diminished tensile strength (30.07 MPa) and Young's modulus (1438.30 MPa), along with an increased elongation percentage (33.98%), when compared to the AP:GE@OTA5%/Ag films.

Figure 11 shows the evolution of the tensile strength (TS) and the elongation at break (EB) parameters of crosslinked films at different mass fractions of OTA. It is evident that as the mass fraction of the crosslinking agent increased, there was a noticeable increase in the tensile strength (TS) accompanied by a decrease of the elongation at break (EB) when compared to the AP:GE film. This is mainly caused by the ability of OTA to increase intermolecular forces along the polymer chains [55]. On the other hand, as the OTA concentration increased, the treated films maintained their transparency but took on a honey-yellow hue when observed with the naked eye, owing to the inherently honey-yellow coloration of the OTA solution. In summary, it could be concluded that both OTA and AgNPs exhibited crosslinking effects on the mechanical properties of the AP:GE films. **3.2.6 Thermogravimetry (TG) measurements**

The thermal behavior of the AP:GE@OTA/Ag films was investigated by thermogravimetric analysis under a nitrogen atmosphere. The obtained TG curves are shown in Figure 12. Three decomposition steps occurred during the thermal degradation of the investigated hydrogel films. Furthermore, the rate of weight loss in these three steps for the AP:GE@OTA/Ag samples was found to be lower than those obtained for the AP:GE film. The first step, which occurred at 50–100°C, is attributed to the adsorbed water evaporation. In the temperature range of 190 to 230°C, corresponding to the second decomposition step, the AP:GE@OTA/Ag samples showed a loss of approximately 30% of their mass, potentially assigned to the thermal oxidation of the films [51]. As the mass fractions of OTA increased in the film, the residual weights exceeded those observed for AP:GE film, which were approximately 30 wt.%. This finding suggests that the incorporation of both OTA and AgNPs within the AP:GE hydrogel network enhances the thermal stability of the blend, due to the formation of strong interactions between the carbonyl groups of OTA and the amino groups of AP and GE through a Schiff base reaction to obtain a new functional group (imine). The final weight loss evidenced at 300–320°C was caused by the final thermal decomposition of the films. The nonvolatile material remaining as a residue at 320°C was found to be around 20% of the original mass of the film sample.

3.2.7 Fluid uptake ability, water retention capacity, and water vapor transmission rate of hydrogel films

To identify suitable wound dressing materials, crucial factors such as fluid uptake ability, water retention capacity, and water vapor transmission rate had to be accurately evaluated.

The fluid uptake capacities of AP:GE@OTA/Ag hydrogel films were assessed by incubating them in PBS at 37 °C. The obtained results are presented in plot (a) of Figure 13. Except for the AP:GE sample, the hydrogel films exhibited similar patterns, in which an equilibrium state of fluid uptake is reached after 2 hours (approximately 90%). Furthermore, both AP-GE and AP:GE@OTA0.5%/Ag films presented lower fluid uptakes compared to the other formulations, which might be attributed to the poor mechanical properties affecting their fluid uptake ability [56]. From plot(a) in Figure 13, there was no notable disparity observed from 2 to 8 hours for the hydrogel films containing OTA and glycerol (acting as a humectant), enabling these films to attain their early saturation in fluid uptake at 2 hours.

The water retention capacities of the hydrogel films were evaluated by measuring the loss of water content when exposed to dry air conditions. The results shown in plot (b) in Figure 13 clearly revealed that the incorporation of both OTA and AgNPs led to an increase in the water retention capacity of the film. Moreover, it was found that these capacities depend on the mass fraction of the crosslinker used during their preparation. Among all the prepared films, the AP:GE@OTA5%/Ag film displayed the highest capacity for retaining water. This can be attributed to the greater rigidity and decreased flexibility of the AP:GE@OTA/Ag macromolecular chains. Besides, the assessment of water retention capacity over 24 hours revealed a sensitive increase when the amount of OTA in the film exceeds 1%. Above this typical value, the change in the capacities is found relatively low (2%-5%), indeed hydrogel films with a rigid structure tend to absorb less fluid, but exhibit a higher percentage of water retention capacity.

Water vapor transmission rate (WVTR) is a critical factor in moisture management in wound areas. In general, it is agreed that a rate of 2000-2500 g/m^2/day water loss can maintain an appropriate level of moisture in wounds without causing dehydration [57]. A lower value results commonly in an accumulation of wound exudates, while a higher WVTR can lead to dehydration of the wound surface. Histograms presenting the obtained WVTR for all the investigated hydrogel films are provided in the plot (c) in Figure 12. Values were found to range from 1653 to 1896 g/m^2/day, which closely align with the suggested range for an optimal wound dressing. Overall, the incorporation of OTA and AgNPs increases the WVTR parameter. As well the increase of the OTA amount in the film until 2% results in an increase of WVTR value. Exceeding this amount, the trend was inversed. This could be attributed to the intensity level of the bonding interactions in the polymer network, along with the presence

of a humectant. Consequently, the prepared biofilms are expected to promote cell migration and facilitate re-epithelialization.

3.10 Biological characterization

The antibacterial efficacy is a crucial requirement for wound dressings intended for use in wound healing. The assessment of antibacterial activity involved the measurement of inhibition zones induced by both AP:GE@OTA and AP:GE@OTA/Ag dressings against S. aureus and E. coli, prevalent pathogens in infected skin wounds. As illustrated in Figure 14, both formulations effectively eliminated surrounding E. coli and S. aureus, while the AP:GE group showed no discernible bacteriostatic effect. With increasing OTA content, the antibacterial zone of AP:GE@OTA dressings consistently expanded. Previous research has demonstrated that TA exhibits a noteworthy inhibitory effect on the growth of both Gram-positive and Gram-negative bacteria, displaying bacteriostatic rather than bactericidal activity [58]. This is attributed to its structural abundance of phenolic hydroxyl groups, recognized for effectively neutralizing free radicals and safeguarding against microorganisms [59]. The AP:GE@OTA/Ag group exhibited significantly larger inhibition zones against both bacterial types, ranging from 12.94±0.23 to 31.77±0.57 mm (Figure 14). This heightened antimicrobial activity is attributed to the synergistic effect of OTA and AgNPs. Interestingly, an inverse relationship was observed between OTA content and the antibacterial zone of AP:GE@OTA/Ag dressings against E.coli and S.aureus. Particularly, the AP:GE@OTA0.5%/Ag dressing showcased the most pronounced bacteriostatic zones, measuring approximately 24.25±0.24 mm and 31.77±0.57 mm for E. coli and S. aureus, respectively. The observed phenomenon is attributed to a change in crosslink density occurring through metal coordination during Ag loading. These findings closely align with outcomes from in vitro silver release studies. The inhibition zone was induced by the diffusion of silver ions, which are trapped within the AP:GE@OTA/Ag matrix, into the surrounding nutrient medium. This diffusion process, facilitated through swollen matrix pores, involves the conversion of Ag^0 to Ag^+ upon exposure to moisture. The resulting Ag^+ ions interact effectively with thiol groups in crucial enzymes linked to bacterial respiration, ultimately leading to cellular demise [60]. In an alternative mechanism, Ag^+ ions may interact with the negatively charged bacterial cell wall, inducing membrane disintegration or interfering with DNA replication, thereby inhibiting bacterial growth. If small enough, AgNPs can penetrate the bacterial cell wall, causing the leakage of cellular constituents and eventual cell death [61]. Overall, these results underscore the potent antibacterial activity of

AP:GE@OTA0.5%/Ag dressings against both bacterial classes, rendering them suitable candidates for selection in in vivo wound healing assays.

Hemocompatibility has emerged as a fundamental criterion for assessing the suitability of biomaterials, particularly when these materials are intended for direct contact with blood in vivo [35]. The standard categorizes biomaterials based on their hemolytic potential: non-hemolytic (0–2% hemolysis), slightly hemolytic (2–5% hemolysis), and hemolytic (>5% hemolysis) [62]. As depicted in Table 5, the HP of the experimental groups tested at 37°C for 2 h is consistently below 2%. This suggests minimal disruption to membrane blood cells, affirming the suitability of all samples for in vitro applications [63]. No significant difference in hemolysis was evident between AP:GE@OTA and AP:GE@OTA/Ag dressings. The lower hemolytic ratio exhibited by these films suggests its enhanced biocompatibility. Therefore, it is noteworthy that the incorporation of OTA and AgNPs does not induce hemolysis, indicating excellent hemocompatibility.

The hemostatic performance of the prepared dressings was also evaluated by a relative parameter, BCI (Figure 15). As well known, the crucial factor of hemostasis is that hemostatic biomaterials demonstrate a potent capability to enhance the enrichment of hemocytes. As depicted in Figure 15, an increase in the duration of blood contact with the samples led to a corresponding decrease in the BCI. As highlighted by Meena et al. [64], blood clotting is related to swelling and rapid water absorption from the blood. This phenomenon contributes to the formation of a concentrated pool of blood components, thereby facilitating the formation of a dense clot.

The AP:GE@OTA0.5%/Ag and AP:GE@OTA5%/Ag films demonstrated a swift decline in BCI within 10 min, whereas the control (Hydrocoll® commercial hydrocolloid dressing), AP:GE@OTA0.5%/, and AP/GE@OTA5% films exhibited a similar trend after 20 min. This observation clearly indicates the capacity of AP:GE@OTA/Ag films to initiate blood coagulation, thus displaying advantageous hemostatic properties. Therefore, the exceptional hemostatic performance of AP:GE@OTA/Ag films may stem from a synergistic effect of AgNPs, attributed to their positive charge [65].

The cytotoxicity of AgNPs has long been widely recognized as a significant challenge in their biomedical applications, prompting extensive research into toxicological mechanisms involved. The cytotoxicity of AgNPs continues to pose a significant challenge in biomedical applications, prompting extensive research to investigate the underlying toxicological mechanisms. Despite considerable efforts, the precise mechanisms and interactions with biological entities remain incompletely understood [66, 67]. The cytotoxicity of AgNPs is

characterized by the release of Ag^+ ions, which interact with cells, affecting DNA and ultimately leading to cell lysis [68]. Studies indicate that smaller AgNPs release elevated concentrations of Ag^+ ions compared to larger counterparts, suggesting size-dependent cytotoxicity [69]. In this context, it is deemed necessary to investigate the release of silver from the AP:GE@OTA/Ag dressings under simulated physiological conditions. Initial silver content was determined through acid digestion and GFAAS analyses, and the results are presented in Table 6. AP:GE@OTA/Ag dressings showed an average loading ranging from 1.02 ± 0.13 to 3.11 ± 0.76 μg/cm^2. Cumulative silver release kinetics, illustrated in Figure 16, showed a biphasic pattern across all AP:GE@OTA/Ag dressings, characterized by an initial burst followed by sustained release. The linear fast release occurred over 2h, succeeded by prolonged release attributed to gradual Ag^+ ion release of from the dressings. After 48h, cumulative silver release percentages from initial loads of AP:GE@OTA0.5%/Ag, AP:GE@OTA1%/Ag, AP:GE@OTA2%/Ag and AP:GE@OTA5%/Ag dressings were 7.18%±0.13%, 3.5%±0.02%, 2.37%±0.01% and 1.66%±0.01%, respectively. This suggests that AP:GE@OTA/Ag dressings effectively control bacterial infection early in wound infliction, providing sustained antibacterial activity over an extended duration. Previous research investigated silver release from various commercial dressings, including ACTICOATTM Flex 3, ACTISORB1 Silver 220, AQUACEL1 Ag, and Mepilex1 Ag. In a serum substitute, silver release ranged from 7% to 67%, with rates varying between 0.0001 μg/(h cm^2) and 4099 μg/(h cm^2) [70]. Another study observed an approximately 86% release of Ag^+ after 48 h from a bacterial cellulose silver nanocomposite immersed in distilled water [71]. In contrast, AP:GE@OTA/Ag dressings, containing only 1.02-3.11 μg/cm^2 of silver, release only 1.63-7.15% of silver after 48h. The low Ag^+ concentrations suggest reduced cytotoxicity, possibly due to AgNPs entrapment and encapsulation within three-dimensional polymeric network [72].

In vitro silver release data were fitted using first-order, Korsmeyer–Peppas, and Sahlin-Peppas models (Figure 17). The Peppas-Sahlin model showed the best fit (Table 7), considering both diffusion and swelling mechanisms. Results indicated dominant diffusion ($n \approx 0.5$) and minimal swelling ($k_2 \rightarrow 0$), suggesting a diffusion-based silver release mechanism. Overall, the results indicate that the crosslinking density of AP:GE@OTA/Ag films effectively controls silver release, making them suitable for sustained-release wound dressings with antibacterial properties.

Assessment of cytocompatibility is deemed a fundamental necessity in biomaterial development for biomedical applications. The cytotoxic effects of the formulated dressings on

the NIT-1 cell line were evaluated at various concentrations over 72-hour period using the XTT assay. Figure 18(a) demonstrates that both AP:GE@OTA0.5% and AP:GE@OTA5% dressings exhibit favorable cell viability and the different OTA concentrations did not affect cell growth. It is recognized that PE, GE and TA are bioactive and biocompatible substances that can effectively enhance cell proliferation [73]. Even with AP:GE@OTA0.5%/Ag and AP:GE@OTA5%/Ag dressings, no obvious cytotoxicity was observed on NIT-1 cells. Notably, AP:GE@OTA0.5%/Ag dressing showed the highest cell viability compared with the other dressings. Statistical analysis revealed significant differences compared to pristine cells. In this study, AgNPs were intentionally reduced by OTA in situ on films, resulting in significantly improved dispersity of the formed AgNPs, thereby reducing cytotoxicity. Further, the changes in cell morphology were examined under a phase contrast microscope (Figure 18(b)). All the tested biopolymeric matrices offered a favorable surface for cell adhesion and growth. Therefore, AP:GE@OTA and AP:GE@OTA/Ag dressings are non-toxic and capable of inducing cell proliferation for wound healing applications. Our findings align with those reported in the literature, where TA and AgNPs were incorporated into a chitosan polymeric matrix [48]. This study demonstrated the enhanced cytocompatibility of CS-Ag-TA cryogel compared to the control, attributed to the presence of AgNPs and TA, which promote cell proliferation and viability.

According to the above experiments, in vivo wound healing studies were conducted on wistar albino rats using AP:GE@OTA5% and AP:GE@OTA0.5%/Ag dressings. Figure 19(a) depicted the comparative decrease in wound area throughout the 12 days. The intricate process of wound healing, wherein the skin barrier regenerates and seals post-injury, operates through a multifaceted mechanism that starts promptly after skin injury. This mechanism involves three interconnected phases, including inflammation, proliferation, and tissue remodeling [74]. The inclusion of bioactive elements capable of impacting these pathways may induce modifications in the wound healing process. Following treatment, all groups exhibited a gradual decrease in wound area. In comparison to the Hydrocoll® group, both AP:GE@OTA5% and AP:GE@OTA0.5%/Ag dressings demonstrated accelerated wound healing, achieving reductions in wound size of 82.13±9.43% and 86.59±2.35%, respectively, within 8 days. Conversely, unhealed wounds were still observable in the AP:GE group, exhibiting a reduction of 57.93±7.10% within the same timeframe. Notably, wounds treated with AP:GE@OTA0.5%/Ag dressings was almost completely closed after 12 days, whereas the skin closure ratio of Hydrocoll® group (control) was 80.87±8.63% (Figure 19(b)). Statistical analysis indicated no significant differences among Hydrocoll®, AP:GE,

AP:GE@OTA5%, and AP:GE@OTA0.5%/Ag treated wounds, potentially attributed to the substantial disparity in standard deviation. The esterified galacturonic acid residues on the AP backbone provide a potent anti-inflammatory effect [75], while gelatin induces hemostasis and supports cell attachment and proliferation, enhancing the wound healing process. Additionally, AgNPs demonstrate strong antimicrobial properties, effectively eradicating bioburden at the wound site, thereby promoting rapid healing. It was noted that the fabricated dressings did not adhere to the wound throughout the application period, allowing for easy removal without harming the skin. Additionally, wounds treated with AP:GE@OTA0.5%/Ag films displayed enhanced tissue quality and reduced scarring (Figure 19(a)). Tummalapallia et al. previously described the development of an in-situ hydrogel wound dressing based on oxidized pectin-gelatin-nanosilver (OP-Gel-NS) [76]. The fundamental crosslinking mechanism employed in the OP-Gel-NS systems mirrors that of the current AP:GE@OTA/Ag systems. Thus, we aimed to compare the efficacity of these two hydrogel films in promoting wound healing. Tummalapallia et al. employed AgNPs as the antimicrobial agent, resulting in approximately 80% healing in 8 days when applied to full thickness excisional wounds on C57BL/6J mice, compared to about 70% in control wounds treated with Bactigras®. On the other hand, wounds treated with AP:GE@OTA0.5%/Ag exhibited a healing rate of 86.59±2.35% within the same timeframe. This comparison suggests that the efficacy of polysaccharide-protein complexes as wound healing matrices, and for tissue regeneration, is greatly affected by the incorporation of OTA and AgNPs as antimicrobial agents.

Conclusions

In summary, the biocompatible AP:GE@OTA/Ag hydrogel films, fabricated through an in-situ crosslinking methodology exhibit significant promise in the realm of wound healing. These biopolymeric dressings demonstrate superior mechanical strength, exceptional water handling features, effective moisture management characteristics, and satisfactory moisture management. The FTIR and XRD analysis testify to the formation of a new biopolymer chemical structure without compatibility issues through the establishment of molecular bonds with the used crosslinker (OTA). SEM/EDX analysis highlighted the formation of a compact network structure and confirmed the successful incorporation of the AgNPs into the film as well. Moreover, TG measurements demonstrated an increase in the thermal stability of the prepared biofilms once the incorporation of the OTA crosslinker and AgNPs is performed. Moreover, the in-situ incorporation of AgNPs as antibacterial agents achieves low cytotoxicity and an excellent antibacterial effect, particularly at an AgNPs loading of 1.02 ± 0.13 μg/cm^2. NIT-1 mouse insulinoma cells displayed favorable cell viability when treated

with both AP:GE@OTA and AP:GE@OTA/Ag dressings. Finally, in-vivo experimentation revealed that the AP:GE@OTA0.5%/Ag facilitated rapid and thorough skin regeneration within 12 days, with no observable tissue toxicity in a Wistar albino rat model. Their efficacy was found better than that of a commercially available dressing (Hydrocoll®). Based on the above advantages, these nanobiocomposite dressings present promising prospects for effective wound management.

List of tables

Table 1

Number of moles of uncrosslinked amino groups ($\times 10^5$) in GE and AP matrices before and after covalent crosslinking, along with the degree of crosslinking determined by TNBS assay. The results present the mean of three determinations ± standard deviation.

	Samples	Number of moles of free amine groups per gram of sample ($\times 10^5$)	Degree of crosslinking (%)
Before crosslinking	GE	31.8 ± 1.35	-
	AP	8.5 ± 0.75	-
	AP:GE	37.3 ± 1.51	-
After crosslinking	AP:GE@OTA0.5%	30.2 ± 1.50	19.03 ± 4.04
	AP:GE@OTA1%	21.3 ± 1.77	42.89 ± 4.76
	AP:GE@OTA2%	15.6 ± 1.00	58.52 ± 2.68
	AP:GE@OTA5%	8.1 ± 1.67	78.27 ± 4.47

Table 2

Angular position of AgNPs diffraction peak, FWHM of the peak and derived particle size from XRD and SEM measurements.

2θ [°]	FWHM (dθ [°])	Particle size from XRD (nm)		Particle size from SEM (nm)
37.72	0.18	47.6	55.62 (as mean value)	57
43.96	0.130	68.8		
64.29	0.163	60.3		
77.40	0.232	45.8		

Table 3

Metal elements contained in AP:GE@OTA/Ag hydrogel films as determined by micro-X-ray fluorescence (μXRF) elemental analysis. They were calculated considering detectable elements.

Hydrogel film	Element (wt.%)				Element (atomic %)			
	S	**Ca**	**Cu**	**Ag**	**S**	**Ca**	**Cu**	**Ag**
AP:GE	74.97	12.21	12.83	00	82.20	10.71	7.10	00
AP:GE@OTA0.5%/Ag	72.99	24.41	2.55	**0.05**	77.80	20.82	1.37	**0.02**
AP:GE@0TA1%/Ag	68.85	18.13	12.95	**0.07**	76.58	16.13	7.27	**0.02**
AP:GE@OTA2%/Ag	56.88	9.96	33.04	**0.12**	69.74	9.77	20.44	**0.04**
AP:GE@OTA5%/Ag	75.31	24.54	0.01	**0.14**	79.28	20.67	00	**0.04**

Table 4
Mechanical properties of the AP:GE@OTA/Ag hydrogel.

Hydrogel film	Thickness (mm)	Tensile Strength (MPa)	Elongation at Break (%)	Young's Modulus (MPa)
AP:GE	0.25±0.07 [a]	17.22±3.50 [a]	45.86±3.43 [a]	838.69±50.74 [a]
AP:GE@OTA0.5%/Ag	0.27±0.07 [a]	23.11±3.35 [a,b]	37.73±1.19 [b]	1218.19±94.56 [b]
AP:GE@OTA1%/Ag	0.34±0.08 [a]	25.33±2.76 [b]	35.43±2.22 [b]	1347.15±46.63 [c]
AP:GE@OTA2%/Ag	0.37±0.08 [a]	30.07±3.49 [b]	33.98±0.96 [b]	1438.30±66.64 [c,d]
AP:GE@OTA5%/Ag	0.41±0.07 [a]	38.49±4.00 [c]	32.42±2.94 [b,c]	1512.98±67.82 [d]

In each column, means sharing the same superscript indicates non-significant differences. Conversely, means labeled with distinct letters indicate statistical differences (p-value < 0.05).
[1] Mean ± SD (n = 5).

Table 5

Hemolytic assay of HRBCs after treatment with distilled water, PBS solution, AP/GE@OTA and AP:GE@OTA/Ag films for 2 h.

Sample	HP (%)
AP:GE	1.39±0.03
AP:GE@OTA0.5%	1.21±0.05
AP:GE@OTA5%	1.52±0.06
AP:GE@OTA0.5%/Ag	1.60±0.06
AP:GE@OTA5%/Ag	1.70±0.12

Table 6

Initial silver loading in AP:GE@OTA/Ag dressings

Dressings	Silver content ($\mu g/cm^2$)	Percentage of silver content (% w/w)
AP:GE@OTA0.5%/Ag	1.02 ± 0.13	0.005
AP:GE@OTA1%/Ag	1.94 ± 0.15	0.009
AP:GE@OTA2%/Ag	2.63 ± 0.37	0.013
AP:GE@OTA5%/Ag	3.11 ± 0.76	0.015

Table 7

Kinetic parameters obtained through fitting to several mathematical kinetic models of silver release profile in in SBF at 37°C, pH 7.4.

Formulation	First order model			Sahlin-Peppas model				Korsmeyer-Peppas model		
	$Mt / M\infty = a[1-exp(-bt)]$			$Mt / M_\infty = K_1t^m + K_2t^{2m}$				$Mt / M_\infty = K_mt^n$		
	a	b	Adj.R^2	K_1	K_2	m	Adj.R^2	K_m	n	Adj.R^2
AP:GE@OTA0.5%	6.16723 ± 0.29314	0.02933 ± 0.00607	0.80695	1.7194 ± 0.22957	-0.10547 ± 0.02786	0.26841 ± 0.0282	0.95857	2.2285 ± 0.23359	0.15382 ± 0.01654	0.91708
AP:GE@OTA1%	3.00107 ± 0.15122	0.03099 ± 0.00688	0.75389	0.92733 ± 0.08727	-0.06269 ± 0.01133	0.2503 ± 0.02089	0.97724	1.1443 ± 0.09177	0.14631 ± 0.01273	0.94322
AP:GE@OTA2%	2.018 ± 0.09607	0.02313 ± 0.00458	0.84487	0.4683 ± 0.06948	-0.02381 ± 0.00696	0.29083 ± 0.03059	0.96	0.62932 ± 0.07419	0.17329 ± 0.01834	0.92168
AP:GE@OTA5%	1.48905 ± 0.06163	0.01853 ± 0.00309	0.89895	0.27419 ± 0.04184	-0.01139 ± 0.0036	0.33161 ± 0.02859	0.96054	0.42413 ± 0.06554	0.18298 ± 0.02387	0.88856

Figures Captions

Figure 1. FTIR (a) and XRDs patterns (b) of PE and AP samples.

Figure 2. ^{1}H-NMR of the soluble PE and AP samples in D2O solvent.

Figure 3. Conversion of AP from pectin.

Figure 4. Digital images of fabricated hydrogel films.

Figure 5. Schematic Illustration of the formation mechanism of AP:GE@OTA/Ag hydrogel film.

Figure 6. Moles of free amino groups (●) and degree of crosslinking (■) in AP and GE matrices before and after crosslinking, as determined via TNBS analysis. Reaction time 30 min, reaction temperature 60°C, pH 5.5.

Figure 7. FTIR Spectra of (a) TA and OTA, (b) AP:GE, AP:GE@OTA5% and AP:GE@OTA5%/Ag films, (c) AP:GE and AP:GE@OTA/Ag hydrogel films.

Figure 8. The X-ray diffractograms of (a) AP:GE@OTA films (b) AP:GE@OTA/Ag films.

Figure 9. (a) SEM images of the surface of AP:GE and AP:GE@OTA/Ag hydrogel films and (b) EDX spectrum of AP:GE@OTA5%/Ag film, confirming the formation of AgNPs.

Figure 10. μXRF spectra validating the incorporation as well as the distribution of AgNPs in AP:GE@OTA5%/Ag hydrogel film.

Figure 11. Effect of OTA content on the tensile properties and elongation at break of AP:GE@OTA/Ag hydrogel films. Gauge length 50 mm; strain rate 50 mm/min.

Figure 12. TG (a) and DTG (b) thermograms of AP:GE and AP:GE@OTA/Ag hydrogel films at heating rate 10 °C/min under nitrogen (100 ml/min).

Figure 13. Fluid uptake ability (a), water retention capacity (b), and water vapor transmission rate (c) of AP:GE@TA/Ag hydrogel films. *p-value < 0.05.

Figure 14. Antimicrobial evaluation by zone of inhibition of AP:GE@OTA and AP:GE@OTA/Ag dressings against E.coli and S.aureus.

Figure 15. Blood coagulation index (BCI) of AP:GE@OTA0.5%. AP:GE@OTA5%. AP:GE@OTA0.5/Ag. AP:GE@OTA5%/Ag and HYDROCOLL® (as a control).

Figure 16. Silver release profiles from AP:GE@OTA/Ag Dressings in SBF at 37°C, pH 7.4.

Figure 17. The silver release kinetics model fitting curves: (a) first-order kinetics model; (b) Sahlin-Peppas model; and (c) Korsmeyer-Peppas model.

Figure 18. (a) In-vitro cell viability analysis assessed by XTT assay against NIT-1 mouse insulinoma cells after 72h. and (b) Cell morphology of NIT-1 after 72h treated with AP:GE@OTA and AP:GE@OTA/Ag dressings at 100 µg/ml. Images were taken with a Nikon eclipse Ts2 phase contrast microscope (20X magnification).

Figure 19. (a) Images of the wound healing process at different time intervals. Wounds treated with Hydrocoll® (commercial product) served as the positive control groups. Full-thickness round wounds (diameter = 3 mm) were created on the cervicodorsal area of Wistar albino rats, (b) wound size reduction with time.

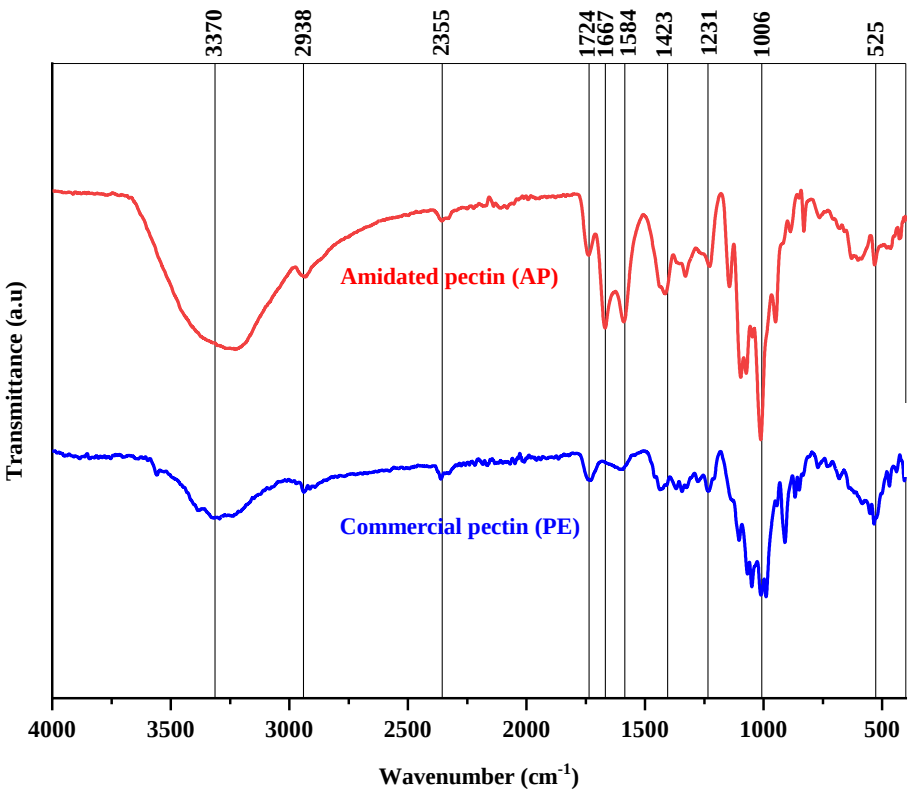

1123

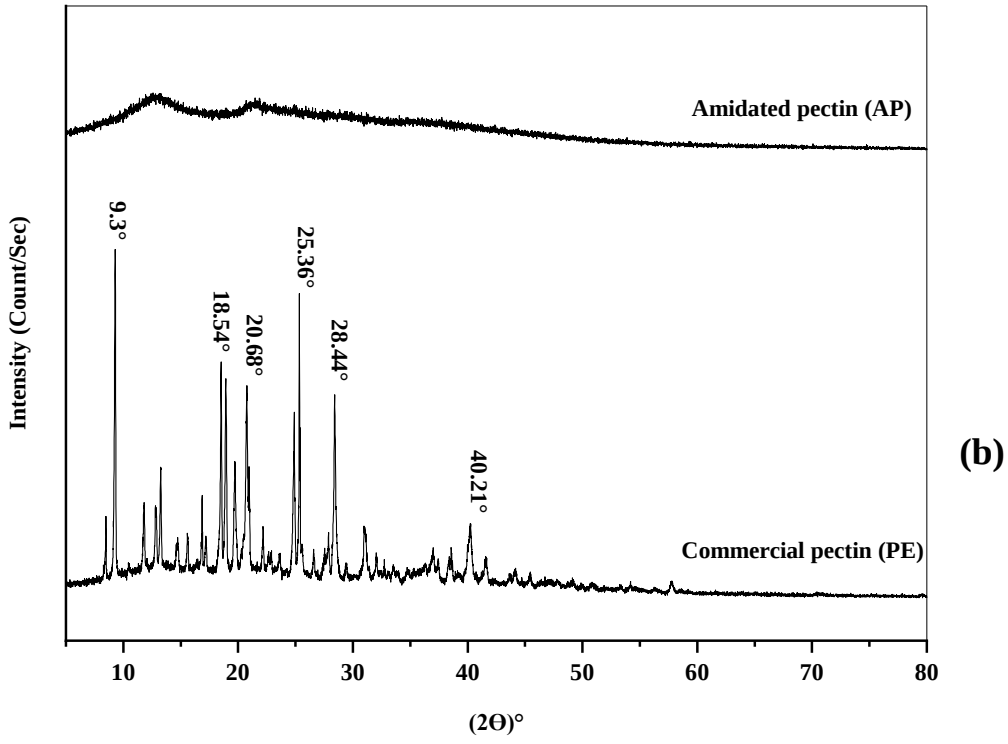

1124

1125 **Figure 1.** FTIR (a) and XRDs patterns (b) of PE and AP samples.
1126

1127

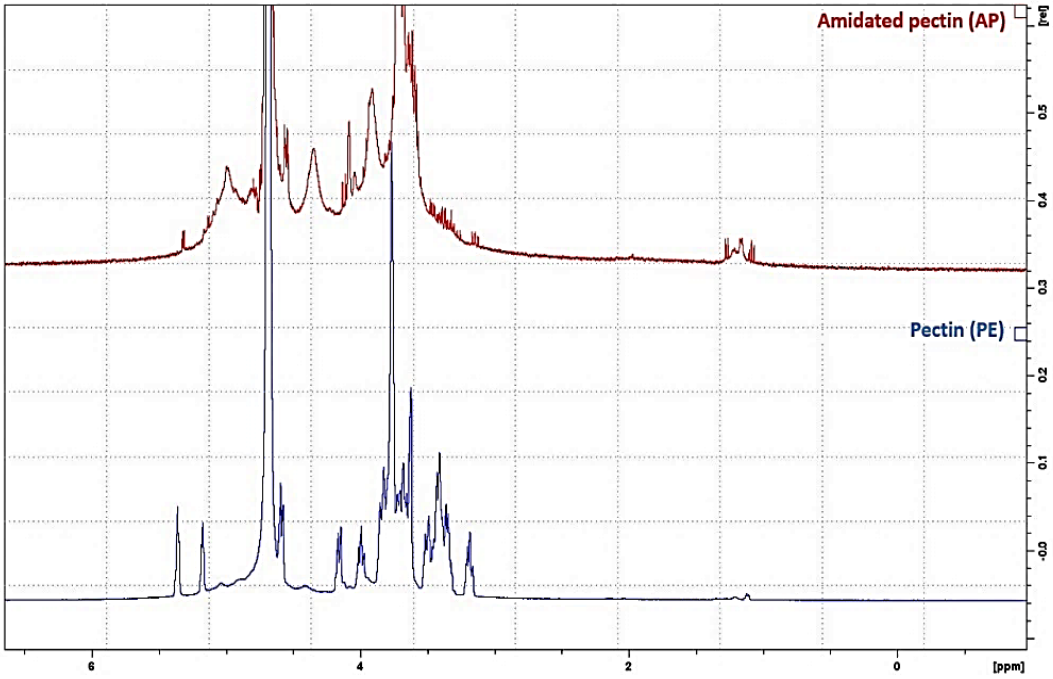

Figure 2. ^{1}H-NMR of the soluble PE and AP samples in D_2O solvent.

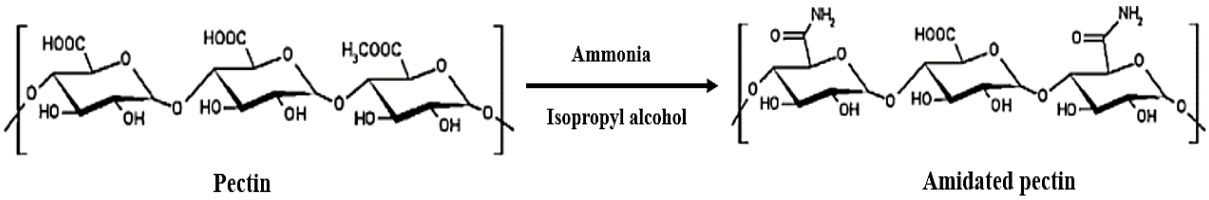

Figure 3. Conversion of AP from pectin.

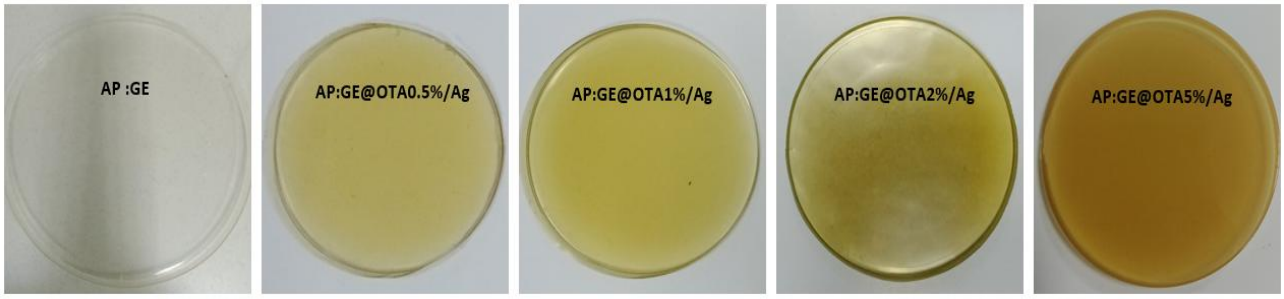

Figure 4. Digital images of fabricated hydrogel films.

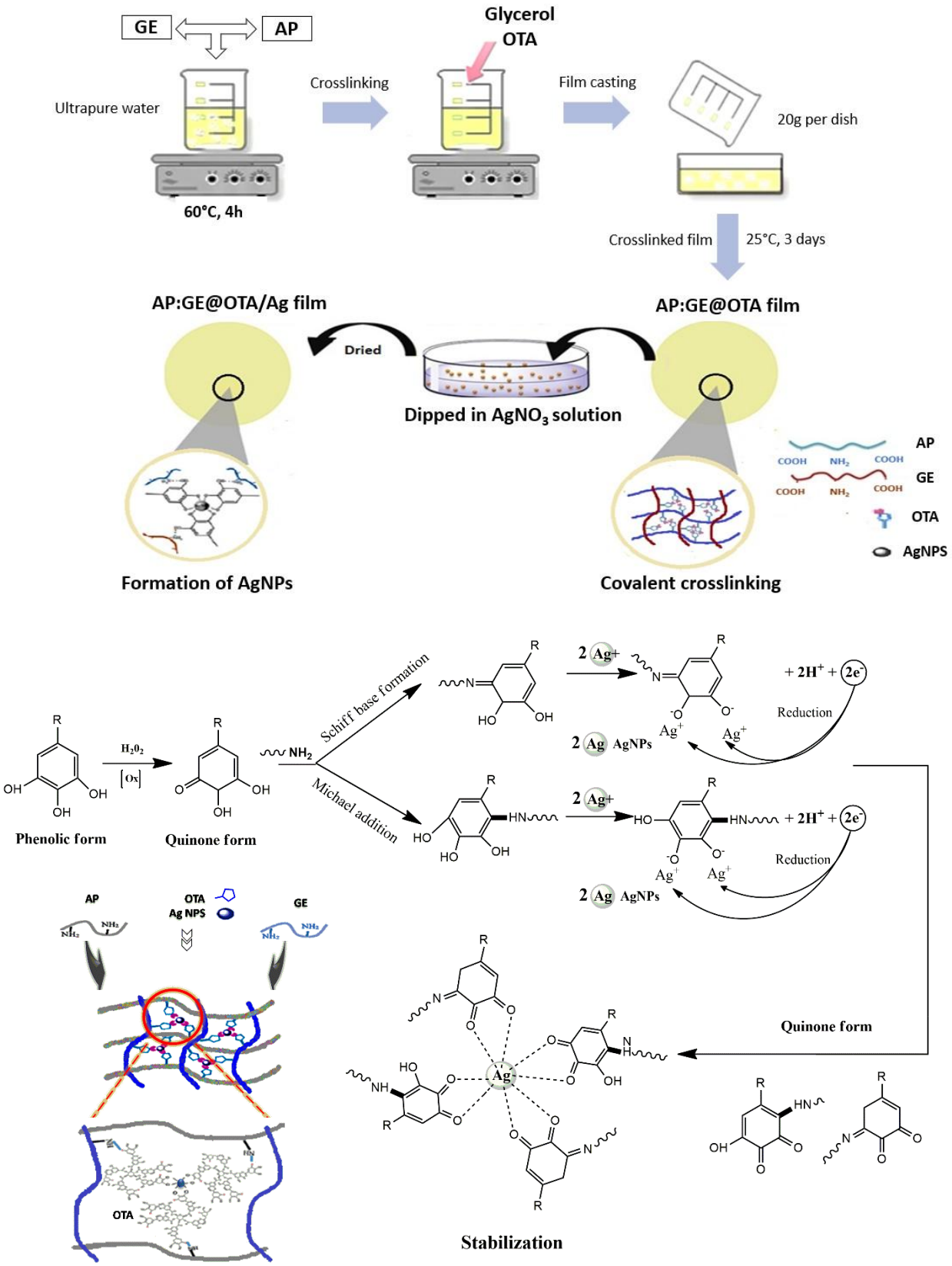

Figure 5. Schematic illustration of the formation mechanism of AP:GE@OTA/Ag hydrogel film.

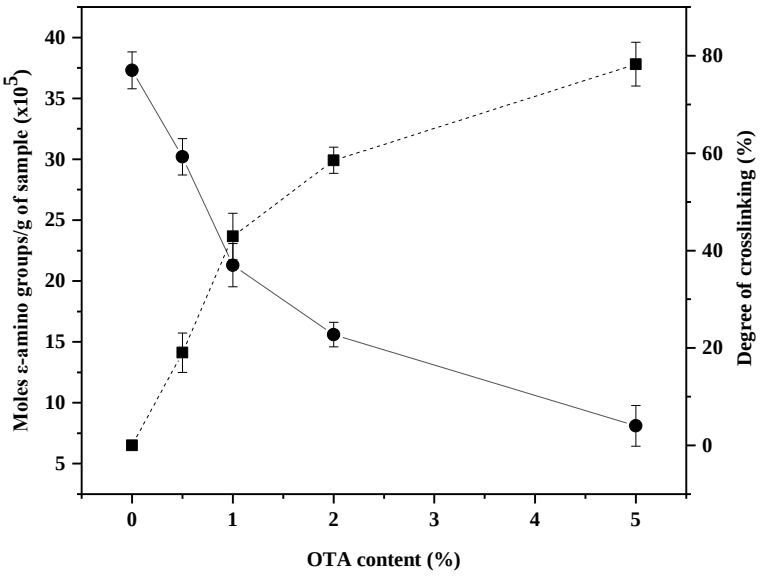

Figure 6. Moles of free amino groups (●) and degree of crosslinking (■) in AP and GE matrices before and after crosslinking, as determined via TNBS analysis. Reaction time 30 min, reaction temperature 60°C, pH 5.5.

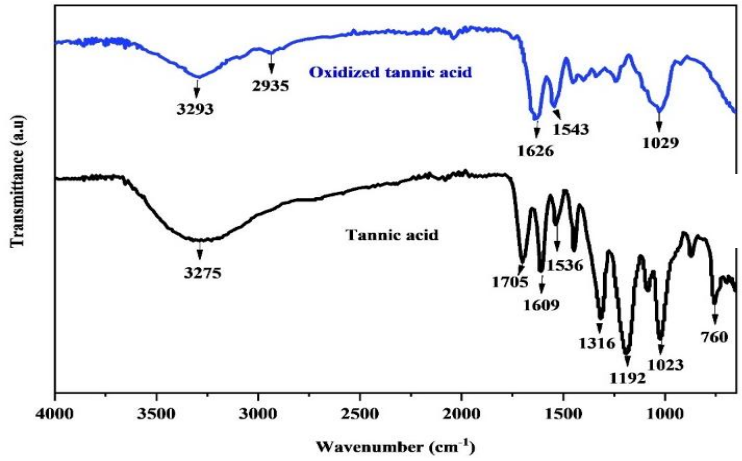

(a)

1210

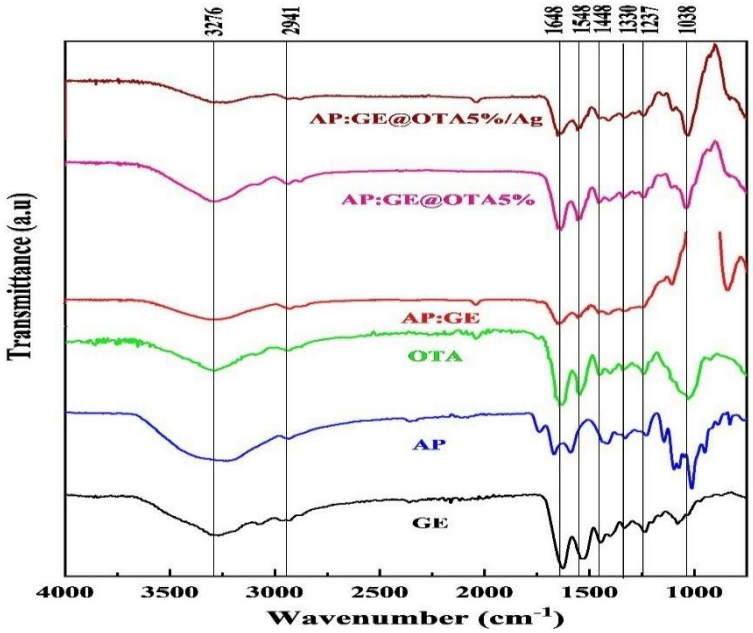

(b)

1211

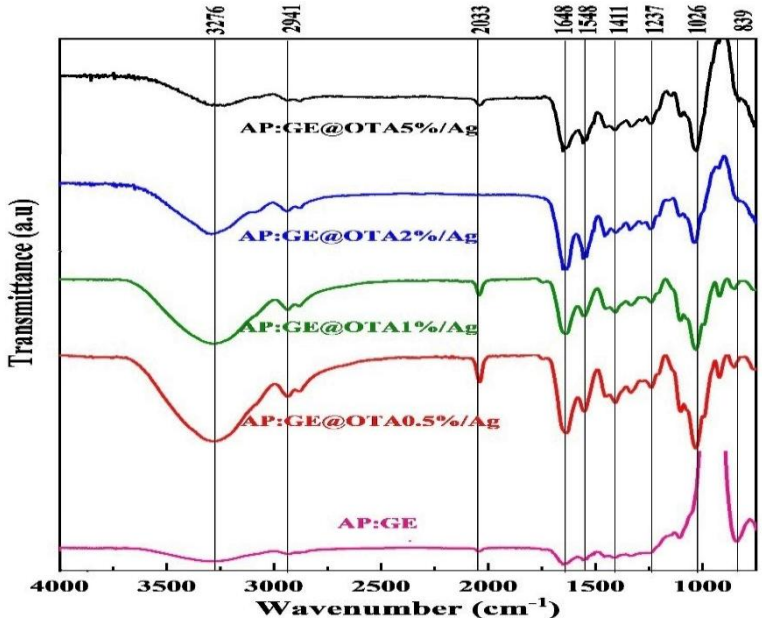

(c)

1212

Figure 7. FTIR Spectra of (a) TA and OTA, (b) AP:GE, AP:GE@OTA5% and AP:GE@OTA5%/Ag films, (c) AP:GE and AP:GE@OTA/Ag hydrogel films.

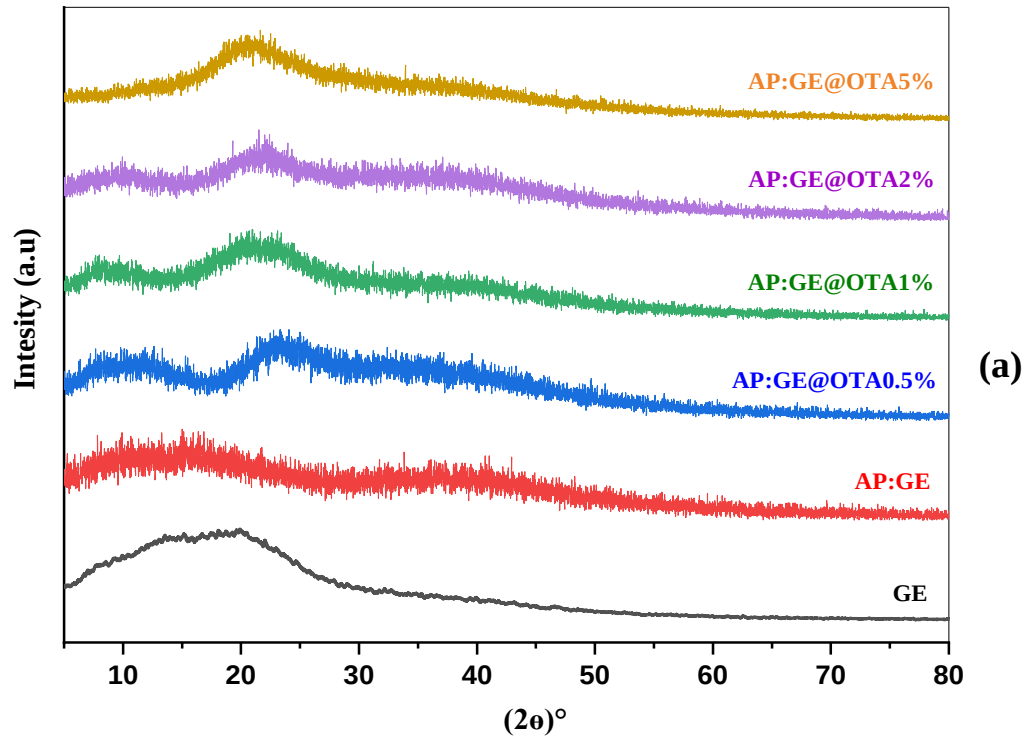

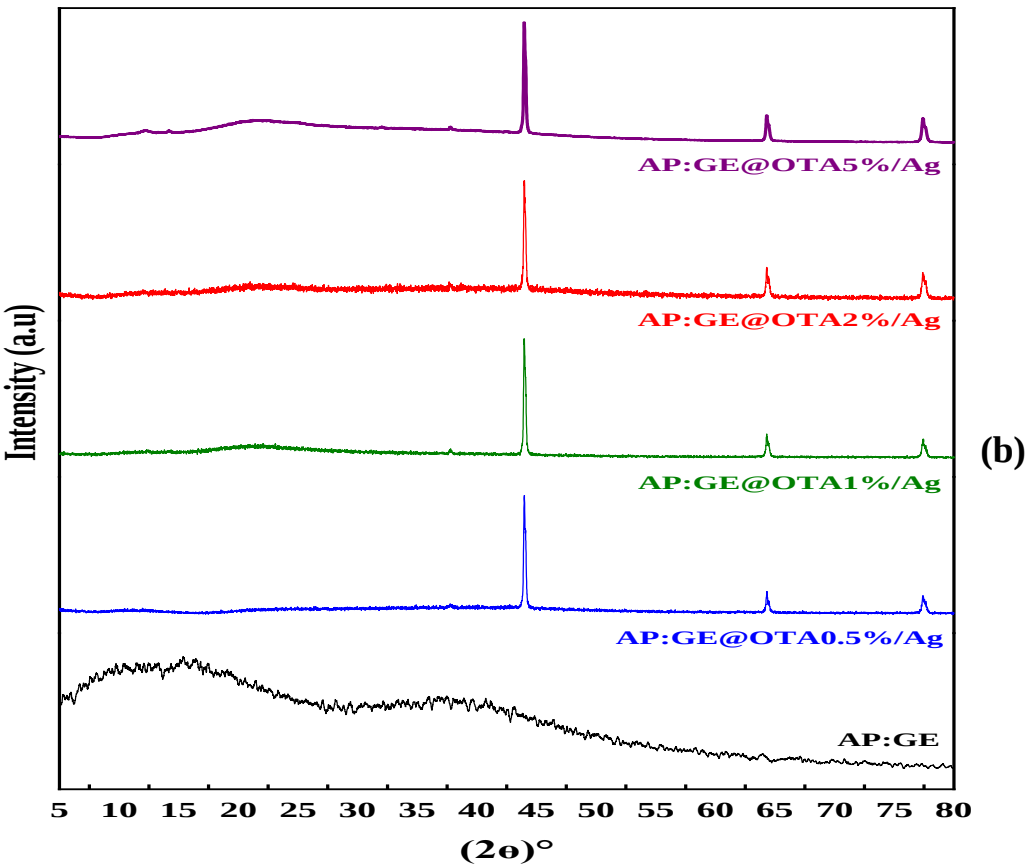

Figure 8. The X-ray diffractograms of (a) AP:GE@OTA films (b) AP:GE@OTA/Ag films.

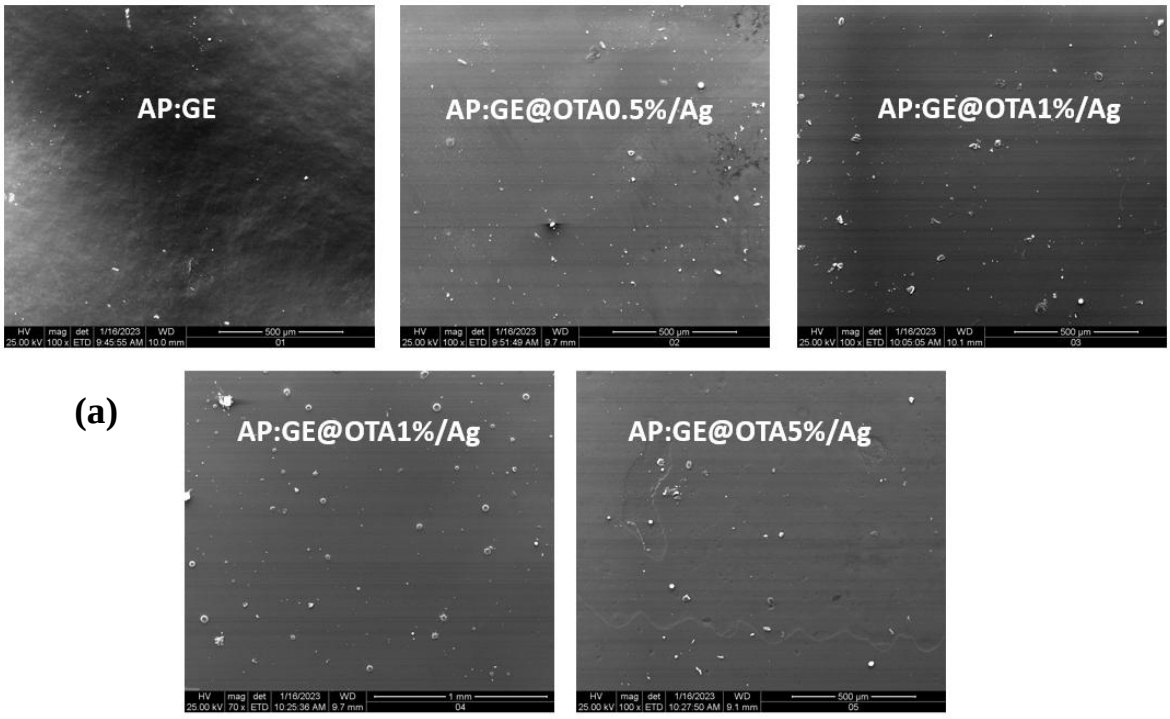

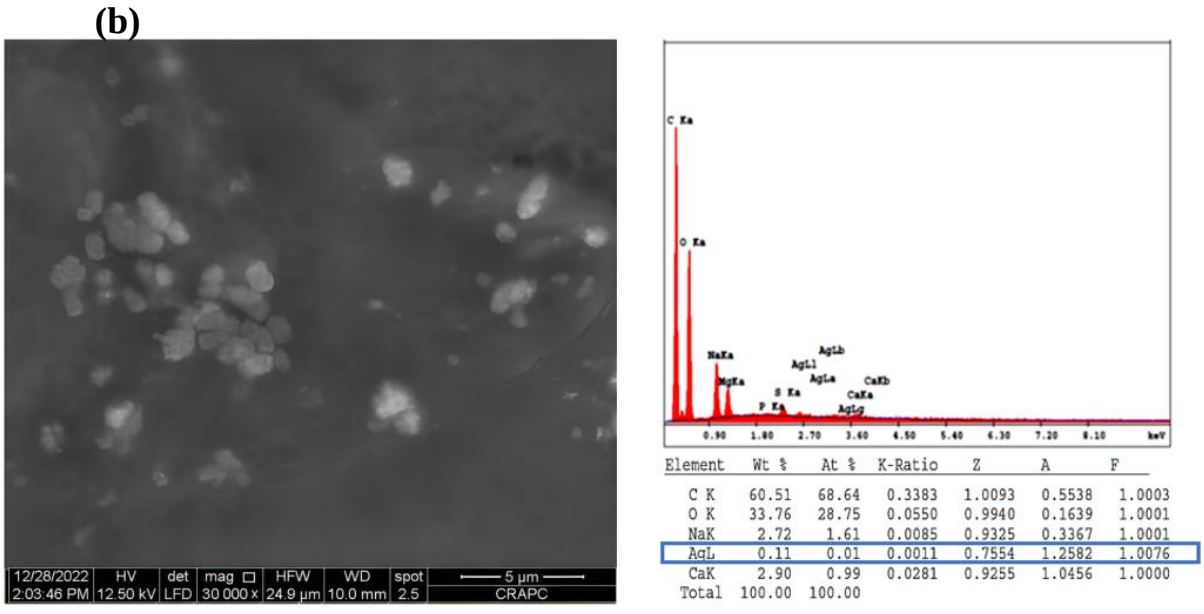

Figure 9. (a) SEM images of the surface of AP:GE and AP:GE@OTA/Ag hydrogel films and (b) EDX spectrum of AP:GE@OTA5%/Ag film, confirming the formation of AgNPs.

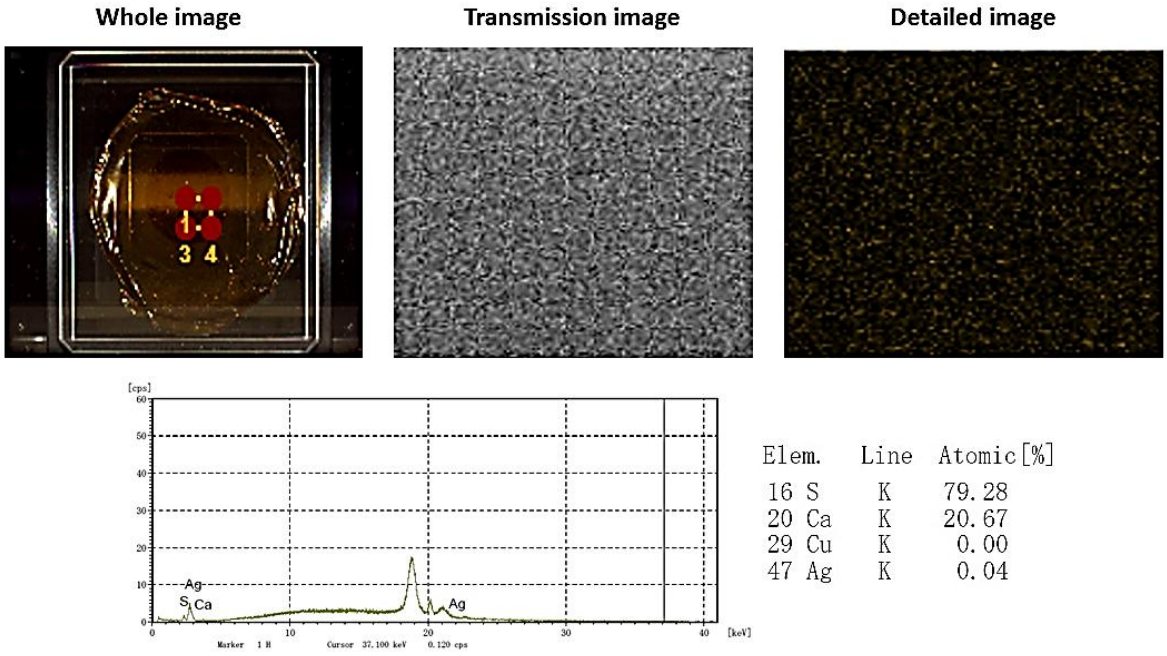

Figure 10. µXRF spectra validating the incorporation as well as the distribution of AgNPs in AP:GE@OTA5%/Ag hydrogel film.

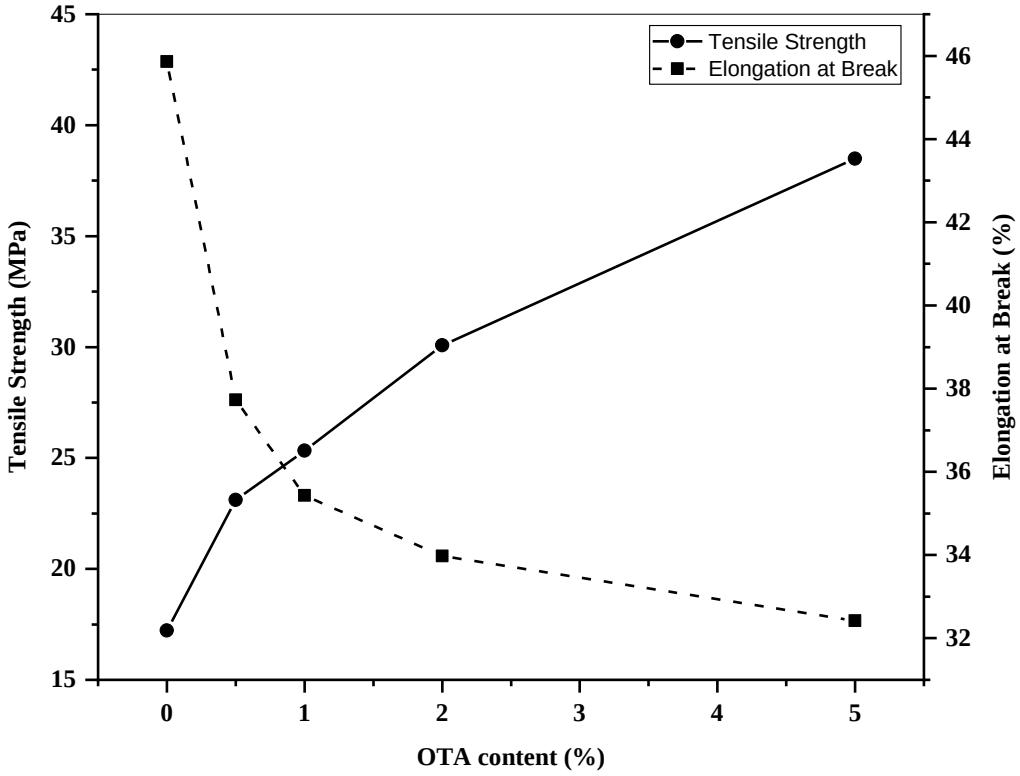

1238

1239 **Figure 11**. Effect of OTA content on the tensile properties and elongation at break of AP:GE@OTA/Ag hydrogel films. Gauge length 50 mm; strain rate 50 mm/min.

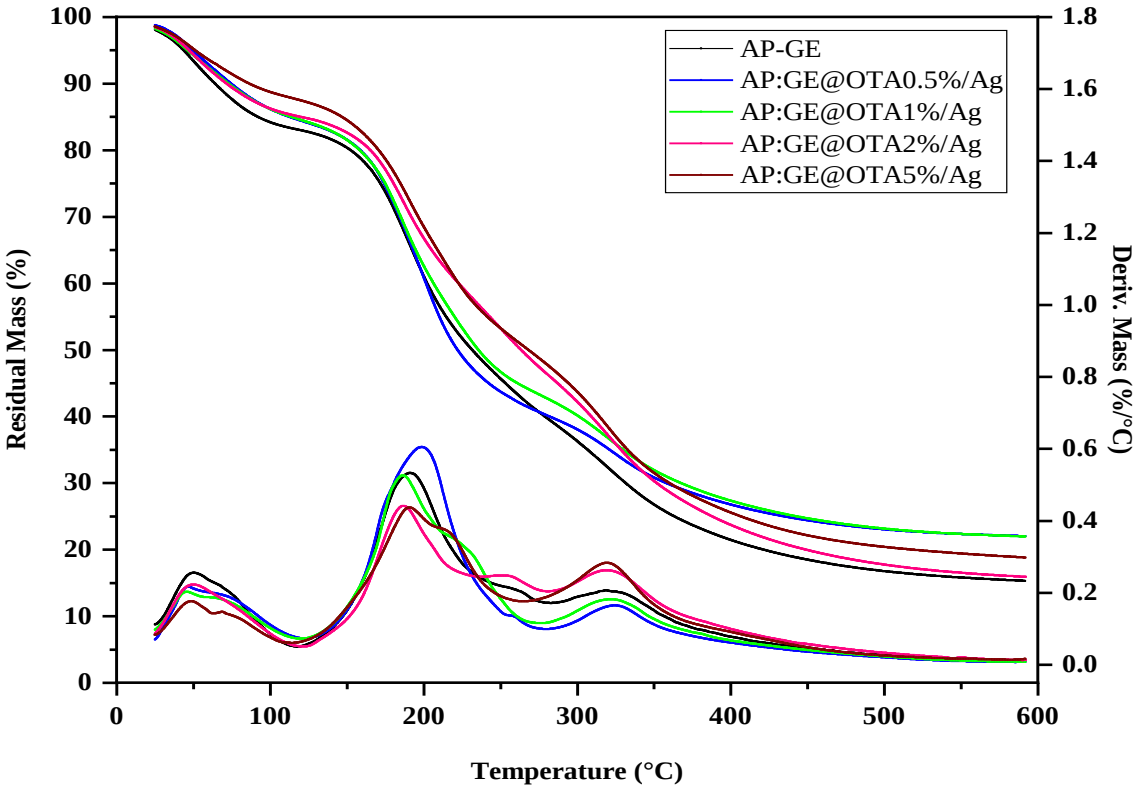

Figure 12. TG (a) and DTG (b) thermograms of AP:GE and AP:GE@OTA/Ag hydrogel films at heating rate 10 °C/min under nitrogen (100 ml/min).

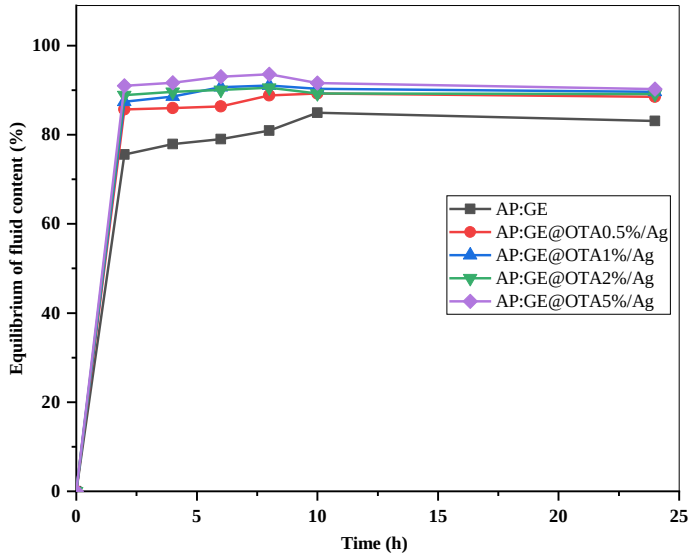

(a)

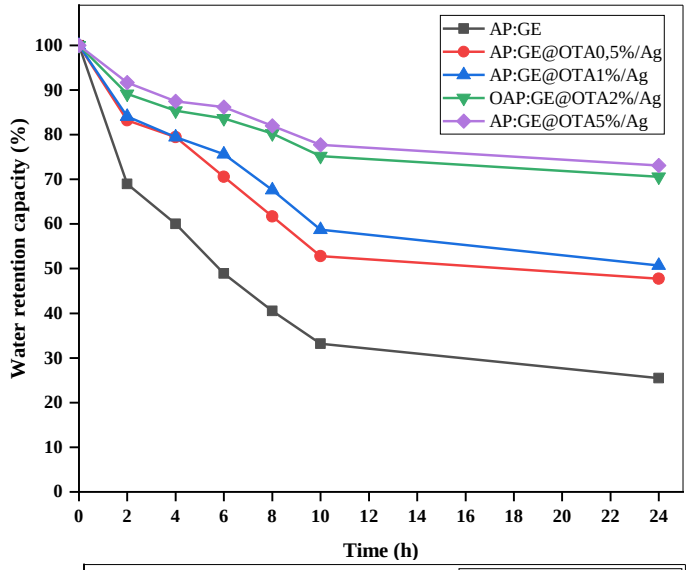

(b)

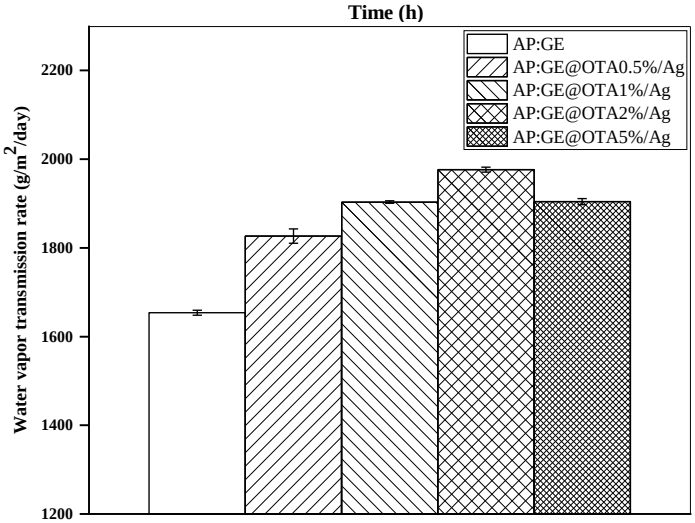

(c)

Figure 13. Fluid uptake ability (a), water retention capacity (b), and water vapor transmission rate (c) of AP:GE@TA/Ag hydrogel films. *p-value < 0.05.

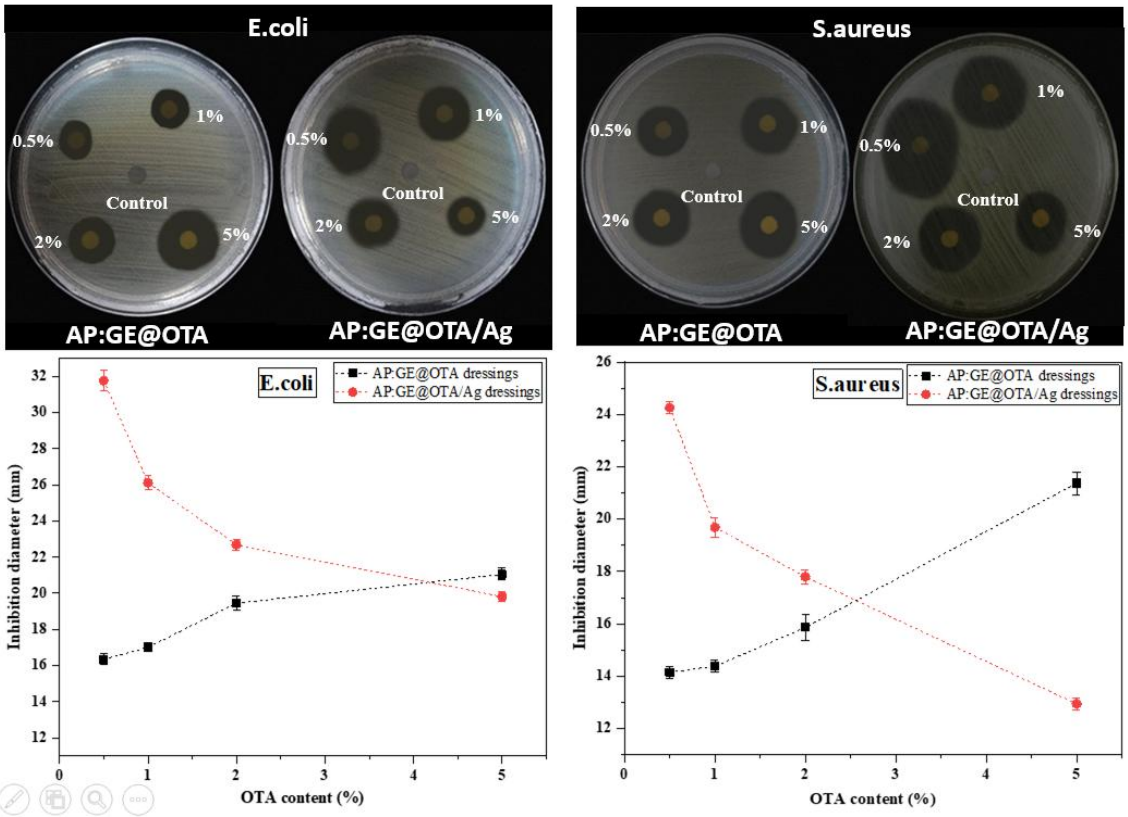

Figure 14. Antimicrobial evaluation by zone of inhibition of AP:GE@OTA and AP:GE@OTA/Ag dressings against E.coli and S.aureus.

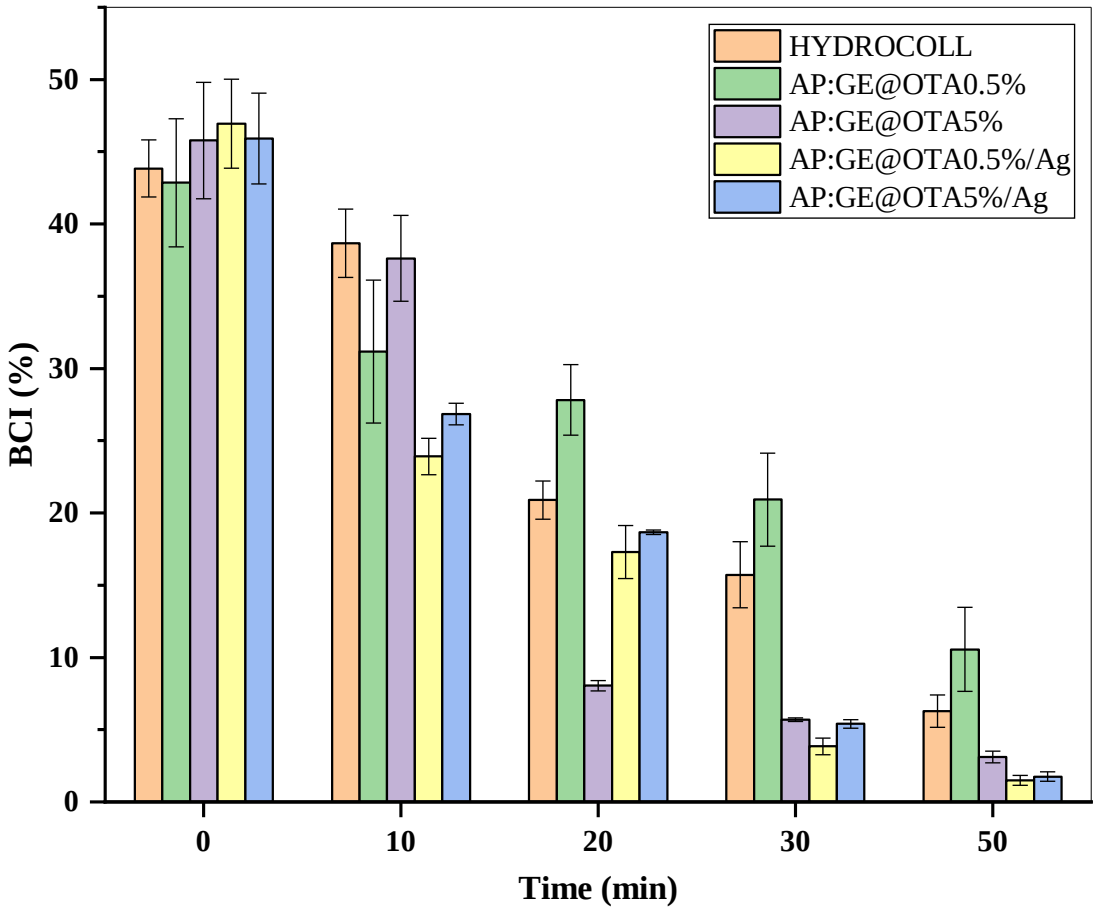

Figure 15. Blood coagulation index (BCI) of AP:GE@OTA0.5%. AP:GE@OTA5%. AP:GE@OTA0.5/Ag. AP:GE@OTA5%/Ag and Hydrocoll® (as a control).

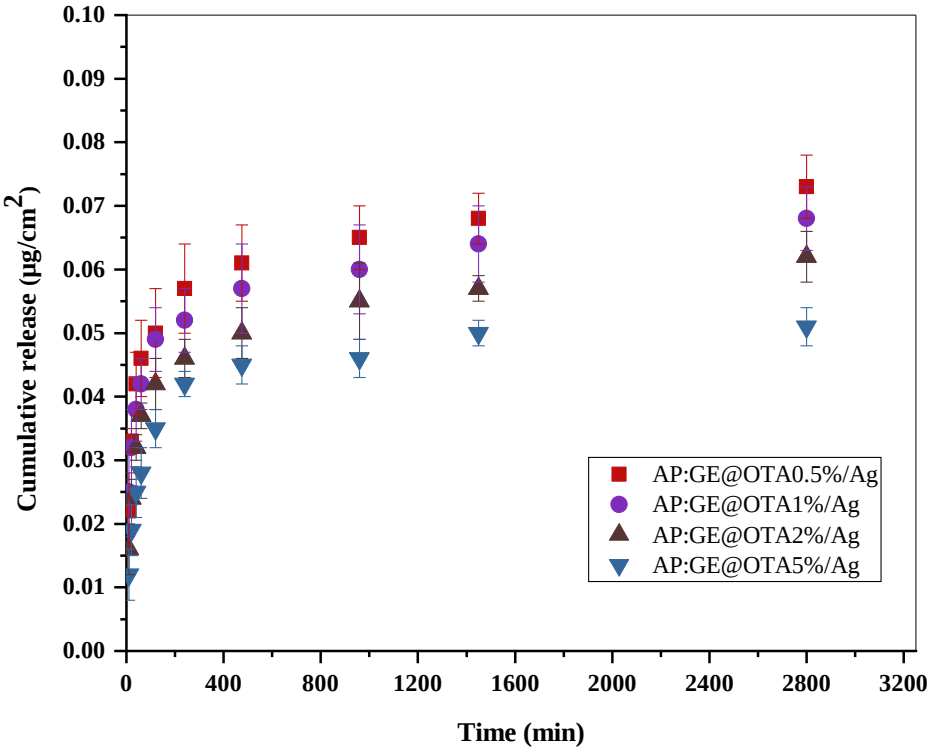

Figure 16. Silver release profiles from AP:GE@OTA/Ag Dressings in SBF at 37°C, pH 7.4.

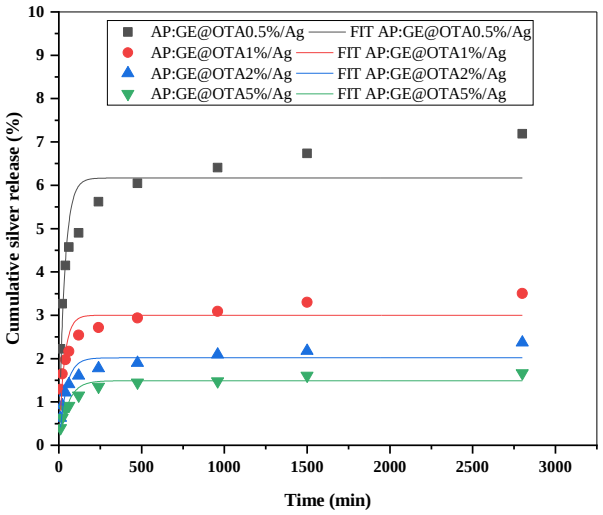

(a)

1314

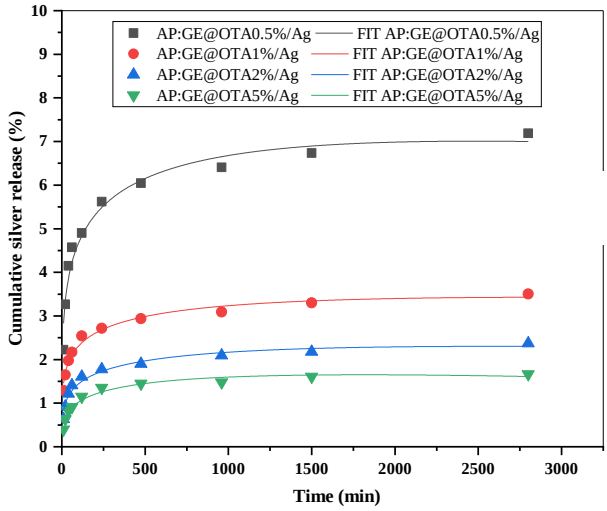

(b)

1315

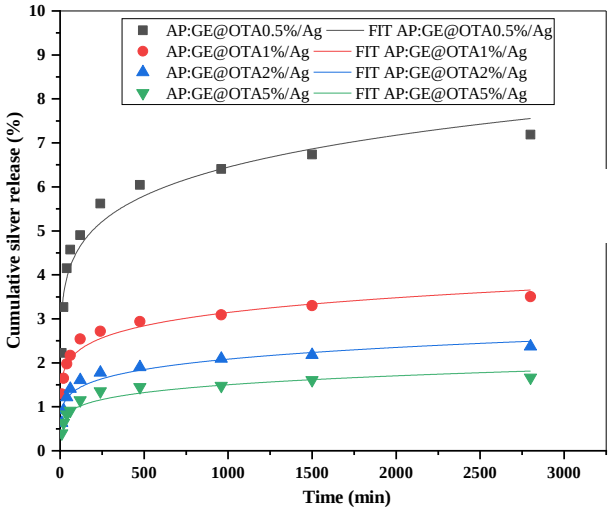

(c)

1316

1317

1318 **Figure 17**. The silver release kinetics model fitting curves: (a) first-order kinetics model; (b) Sahlin-Peppas model; and (c) Korsmeyer-Peppas model.

1319

1320

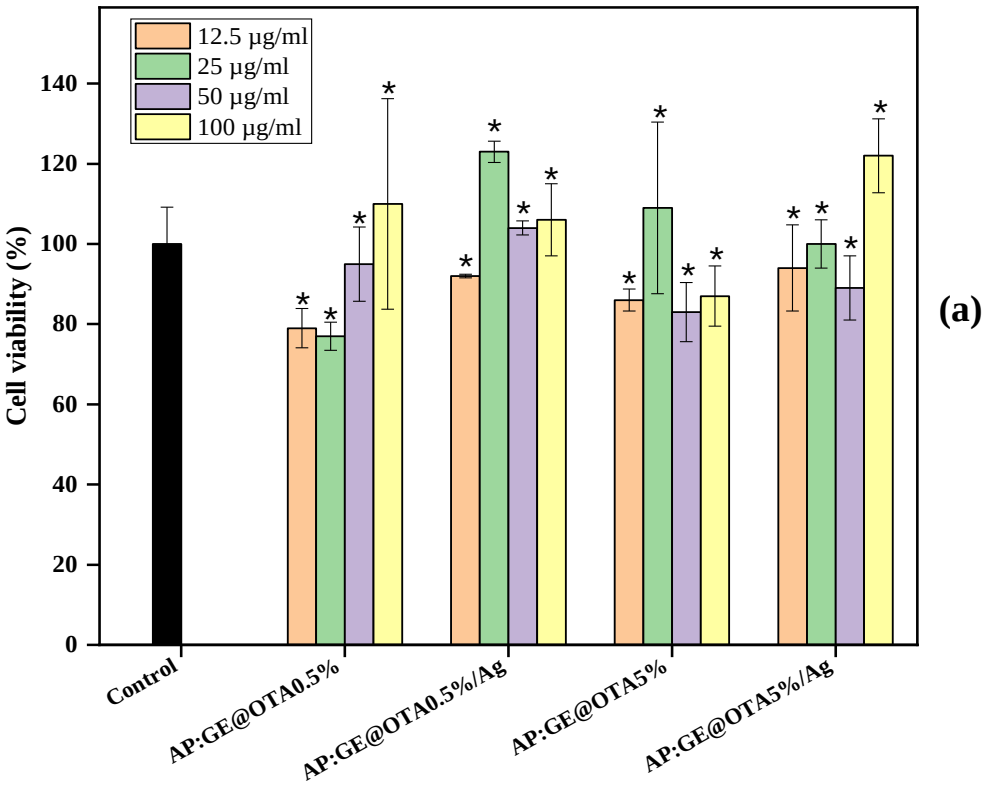

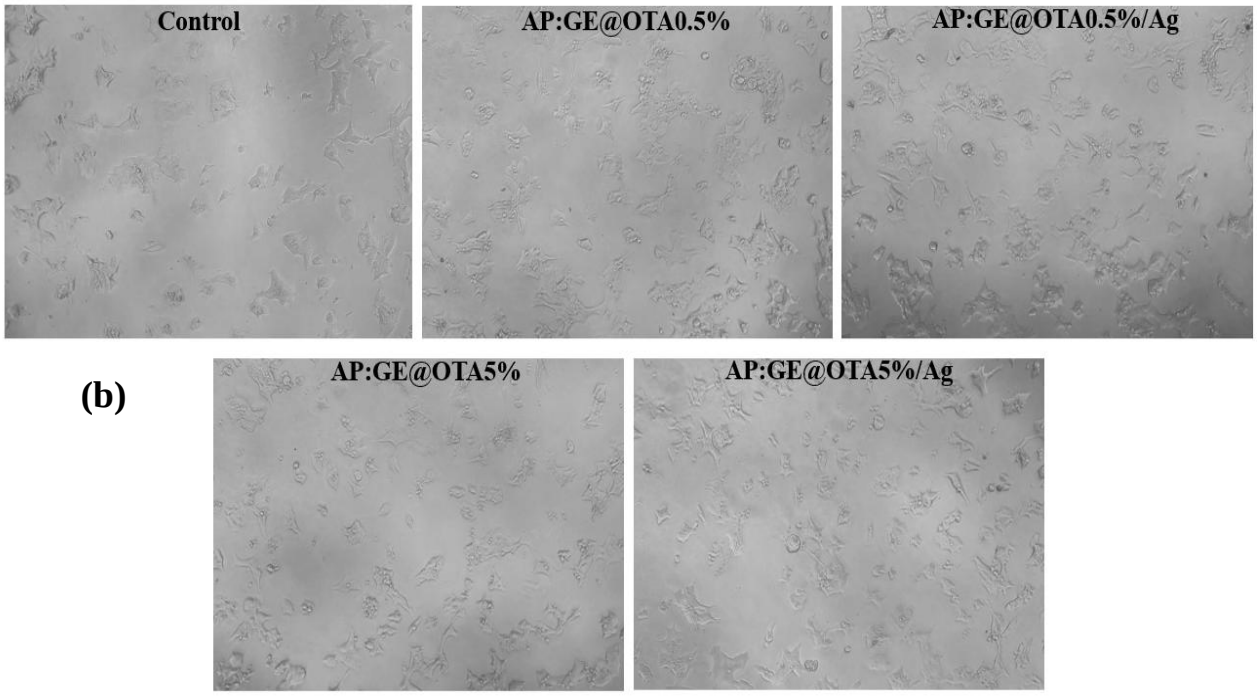

Figure 18. (a) In-vitro cell viability analysis assessed by XTT assay against NIT-1 mouse insulinoma cells after 72h. and (b) Cell morphology of NIT-1 after 72h treated with AP:GE@OTA and AP:GE@OTA/Ag dressings at 100 µg/ml. Images were taken with a Nikon eclipse Ts2 phase contrast microscope (20X magnification).

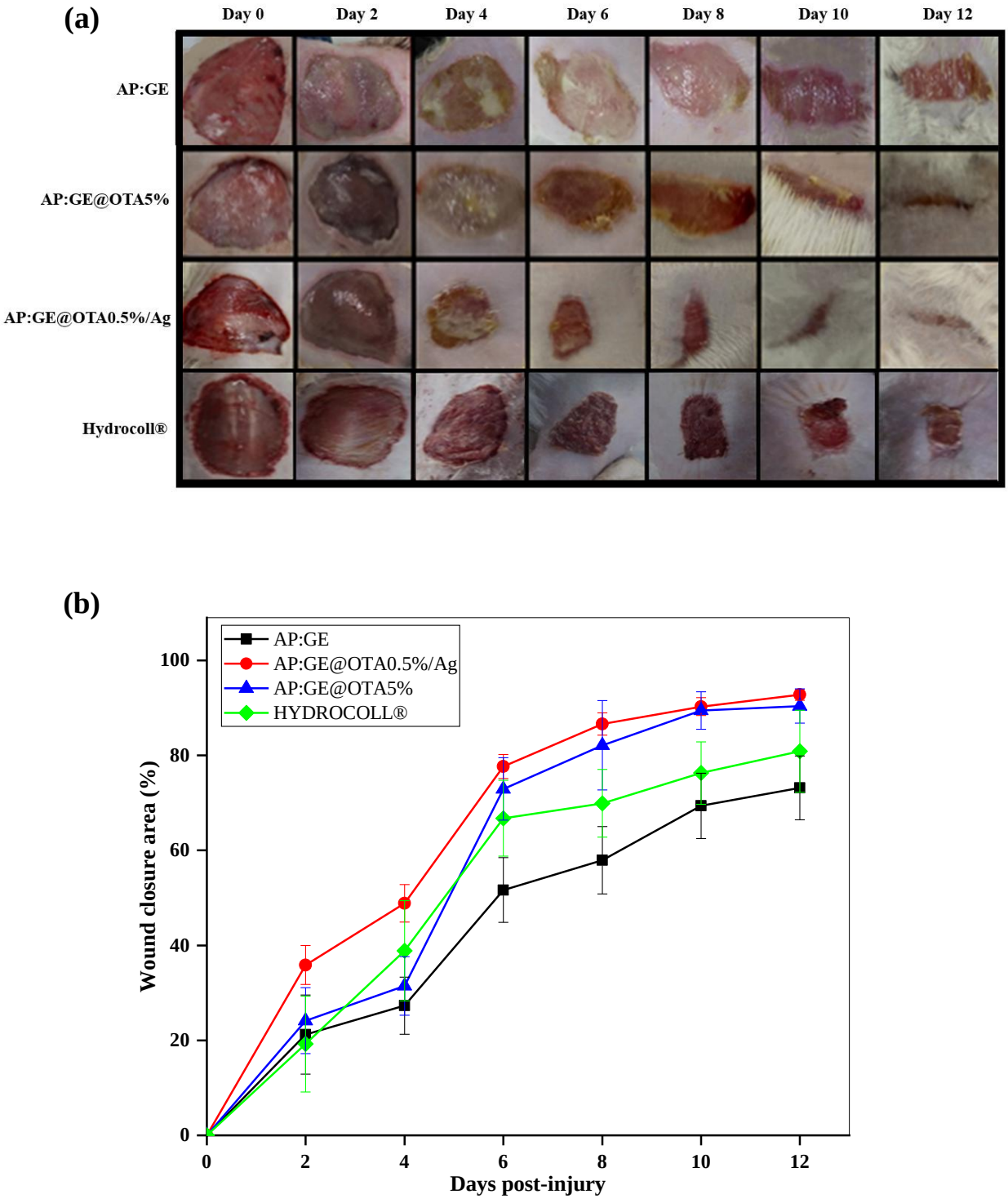

Figure 19. (a) Images of the wound healing process at different time intervals. Wounds treated with Hydrocoll® (commercial product) served as the positive control groups. Full-thickness round wounds (diameter = 3 mm) were created on the cervicodorsal area of Wistar albino rats, (b) wound size reduction with time.

References

[1] J. Zhu, H. Zhou, E.M. Gerhard, S. Zhang, F.I.P. Rodríguez, T. Pan, H. Yang, Y. Lin, J. Yang, H. Cheng, Smart bioadhesives for wound healing and closure, Bioactive Materials 19 (2023) 360-375.

[2] X. Bao, Q. Zhu, Y. Chen, H. Tang, W. Deng, H. Guo, L. Zeng, Antibacterial and antioxidant films based on HA/Gr/TA fabricated using electrospinning for wound healing, International Journal of Pharmaceutics 626 (2022) 122139.

[3] K. Souliotis, I. Kalemikerakis, M. Saridi, M. Papageorgiou, A. Kalokerinou, A cost and clinical effectiveness analysis among moist wound healing dressings versus traditional methods in home care patients with pressure ulcers, Wound Repair and Regeneration 24(3) (2016) 596-601.

[4] R. Gobi, P. Ravichandiran, R.S. Babu, D.J. Yoo, Biopolymer and synthetic polymer-based nanocomposites in wound dressing applications: a review, Polymers 13(12) (2021) 1962.

[5] A. Saikia, N. Karak, Introduction to biodegradable and biocompatible polymer nanocomposites: synthesis, structure, fundamental properties, biocompatibility, and biodegradability, Biodegradable and Biocompatible Polymer Nanocomposites, Elsevier2023, pp. 1-34.

[6] A.A. Hafiza, M.K. Khairunnisa-Atiqah, N.S.N. Mazlan, K.M. Salleh, S. Zakaria, Biocompatible and biodegradable materials in medical applications, Green Sustainable Process for Chemical and Environmental Engineering and Science, Elsevier2023, pp. 331-358.

[7] A. Lapomarda, G. Cerqueni, M.A. Geven, I. Chiesa, A. De Acutis, M. De Blasi, F. Montemurro, C. De Maria, M. Mattioli-Belmonte, G. Vozzi, Physicochemical Characterization of Pectin-Gelatin Biomaterial Formulations for 3D Bioprinting, Macromolecular Bioscience 21(9) (2021) 2100168.

[8] N.S. Bostancı, S. Büyüksungur, N. Hasirci, A. Tezcaner, pH responsive release of curcumin from photocrosslinked pectin/gelatin hydrogel wound dressings, Biomaterials Advances 134 (2022) 112717.

[9] K. Osetrov, M. Uspenskaya, V. Sitnikova, The influence of oxidant on gelatin–tannin hydrogel properties and structure for potential biomedical application, Polymers 14(1) (2021) 150.

[10] J. Yang, M. Li, Y. Wang, H. Wu, T. Zhen, L. Xiong, Q. Sun, Double cross-linked chitosan composite films developed with oxidized tannic acid and ferric ions exhibit high strength and excellent water resistance, Biomacromolecules 20(2) (2019) 801-812.

[11] C.M.P. Freitas, J.S.R. Coimbra, V.G.L. Souza, R.C.S. Sousa, Structure and applications of pectin in food, biomedical, and pharmaceutical industry: A review, Coatings 11(8) (2021) 922.

[12] T. Li, M. Sun, S. Wu, State-of-the-art review of electrospun gelatin-based nanofiber dressings for wound healing applications, Nanomaterials 12(5) (2022) 784.

[13] S. Dumitriu, V.I. Popa, Polymeric biomaterials, CRC Press2013.

[14] B. Gupta, M. Tummalapalli, B. Deopura, M. Alam, Preparation and characterization of in-situ crosslinked pectin–gelatin hydrogels, Carbohydrate polymers 106 (2014) 312-318.

[15] P. Jantrawut, J. Bunrueangtha, J. Suerthong, N. Kantrong, Fabrication and characterization of low methoxyl pectin/gelatin/carboxymethyl cellulose absorbent hydrogel film for wound dressing applications, Materials 12(10) (2019) 1628.

[16] A. Chetouani, M. Elkolli, H. Haffar, H. Chader, F. Riahi, T. Varacavoudin, D. Le Cerf, Multifunctional hydrogels based on oxidized pectin and gelatin for wound healing improvement, International Journal of Biological Macromolecules 212 (2022) 248-256.

[17] X. Shi, S. Cui, X. Song, A.P. Rickel, H.J. Sanyour, J. Zheng, J. Hu, Z. Hong, Y. Zhou, Y. Liu, Gelatin-crosslinked pectin nanofiber mats allowing cell infiltration, Materials Science and Engineering: C 112 (2020) 110941.

[18] M.A. Pujana, L. Pérez-Álvarez, L.C.C. Iturbe, I. Katime, Biodegradable chitosan nanogels crosslinked with genipin, Carbohydrate Polymers 94(2) (2013) 836-842.

[19] N. Reddy, R. Reddy, Q. Jiang, Crosslinking biopolymers for biomedical applications, Trends in biotechnology 33(6) (2015) 362-369.

[20] Z. Guo, W. Xie, J. Lu, X. Guo, J. Xu, W. Xu, Y. Chi, N. Takuya, H. Wu, L. Zhao, Tannic acid-based metal phenolic networks for bio-applications: a review, Journal of Materials Chemistry B 9(20) (2021) 4098-4110.

[21] W. Jing, C. Xiaolan, C. Yu, Q. Feng, Y. Haifeng, Pharmacological effects and mechanisms of tannic acid, Biomedicine & Pharmacotherapy 154 (2022) 113561.
[22] K. Juby, C. Dwivedi, M. Kumar, S. Kota, H. Misra, P. Bajaj, Silver nanoparticle-loaded PVA/gum acacia hydrogel: Synthesis, characterization and antibacterial study, Carbohydrate polymers 89(3) (2012) 906-913.
[23] T. Ahmad, Reviewing the tannic acid mediated synthesis of metal nanoparticles, Journal of Nanotechnology 2014 (2014).
[24] S. Ravindra, A.F. Mulaba-Bafubiandi, V. Rajinikanth, K. Varaprasad, N. Narayana Reddy, K. Mohana Raju, Development and characterization of curcumin loaded silver nanoparticle hydrogels for antibacterial and drug delivery applications, Journal of Inorganic and Organometallic Polymers and Materials 22 (2012) 1254-1262.
[25] J. Reitsma, J. Thibault, W. Pilnik, Properties of amidated pectins. I. Preparation and characterization of amidated pectins and amidated pectic acids, Food Hydrocolloids 1(2) (1986) 121-127.
[26] K. Osetrov, M. Uspenskaya, V. Sitnikova, The influence of oxidant on gelatin–tannin hydrogel properties and structure for potential biomedical application, Polymers 14(1) (2022) 150.
[27] N. Xu, Y. Yuan, L. Ding, J. Li, J. Jia, Z. Li, D. He, Y. Yu, Multifunctional chitosan/gelatin@ tannic acid cryogels decorated with in situ reduced silver nanoparticles for wound healing, Burns & Trauma 10 (2022) tkac019.
[28] A. Sinitsya, J. Čopíková, V. Prutyanov, S. Skoblya, V. Machovič, Amidation of highly methoxylated citrus pectin with primary amines, Carbohydrate polymers 42(4) (2000) 359-368.
[29] A.S.A. Habeeb, Determination of free amino groups in proteins by trinitrobenzenesulfonic acid, Analytical biochemistry 14(3) (1966) 328-336.
[30] I. Ofner, Clyde M, W.A. Bubnis, Chemical and swelling evaluations of amino group crosslinking in gelatin and modified gelatin matrices, Pharmaceutical research 13 (1996) 1821-1827.
[31] A.S.D.o.M. Properties, Standard test method for tensile properties of thin plastic sheeting, American Society for Testing and Materials, 1995.
[32] B. Balakrishnan, M. Mohanty, P. Umashankar, A. Jayakrishnan, Evaluation of an in situ forming hydrogel wound dressing based on oxidized alginate and gelatin, Biomaterials 26(32) (2005) 6335-6342.
[33] A. ASTM, Standard E96–00. Standard test methods for water vapour transmission of materials, Annual Book of ASTM Standards 4 (2000).
[34] A. Sharma, C. Verma, S. Mukhopadhyay, A. Gupta, B. Gupta, Silver nanoparticle-embedded nanogels for infection-resistant surfaces, ACS Applied Nano Materials 5(6) (2022) 8546-8556.
[35] S. Wang, R. Castro, X. An, C. Song, Y. Luo, M. Shen, H. Tomás, M. Zhu, X. Shi, Electrospun laponite-doped poly (lactic-co-glycolic acid) nanofibers for osteogenic differentiation of human mesenchymal stem cells, Journal of Materials Chemistry 22(44) (2012) 23357-23367.
[36] Q.Z. Wang, X.G. Chen, Z.X. Li, S. Wang, C.S. Liu, X.H. Meng, C.G. Liu, Y.H. Lv, L.J. Yu, Preparation and blood coagulation evaluation of chitosan microspheres, Journal of Materials Science: Materials in Medicine 19 (2008) 1371-1377.
[37] B. Gupta, M. Kumari, S. Ikram, Drug release studies of N-isopropyl acrylamide/acrylic acid grafted polypropylene nonwoven fabric, Journal of Polymer Research 20 (2013) 1-6.
[38] L. Jost, J. Kirkwood, T. Whiteside, Improved short-and long-term XTT-based colorimetric cellular cytotoxicity assay for melanoma and other tumor cells, Journal of immunological methods 147(2) (1992) 153-165.
[39] P. Singh, C. Verma, S. Mukhopadhyay, A. Gupta, B. Gupta, Preparation of thyme oil loaded κ-carrageenan-polyethylene glycol hydrogel membranes as wound care system, International Journal of Pharmaceutics 618 (2022) 121661.
[40] R.K. Mishra, M. Datt, K. Pal, A. Banthia, Preparation and characterization of amidated pectin based hydrogels for drug delivery system, Journal of Materials Science: Materials in Medicine 19 (2008) 2275-2280.

[41] J.-L. Gong, X.-Y. Wang, G.-M. Zeng, L. Chen, J.-H. Deng, X.-R. Zhang, Q.-Y. Niu, Copper (II) removal by pectin–iron oxide magnetic nanocomposite adsorbent, Chemical Engineering Journal 185 (2012) 100-107.
[42] C. Li, H. Nie, Y. Chen, Z.Y. Xiang, J.B. Li, Amide pectin: A carrier material for colon-targeted controlled drug release, Journal of Applied Polymer Science 133(29) (2016).
[43] Y. Zhuang, Z. Guo, Q. Zhang, J. Liu, P. Fei, B. Huang, Preparation of functionalized pectin through acylation with alkyl gallates: Experiments coupled with density functional theory, International Journal of Biological Macromolecules 202 (2022) 278-285.
[44] W.A. Bubnis, C.M. Ofner III, The determination of ϵ-amino groups in soluble and poorly soluble proteinaceous materials by a spectrophotometrie method using trinitrobenzenesulfonic acid, Analytical biochemistry 207(1) (1992) 129-133.
[45] R. Sashidhar, A. Capoor, D. Ramana, Quantitation of ϵ-amino group using amino acids as reference standards by trinitrobenzene sulfonic acid: A simple spectrophotometric method for the estimation of hapten to carrier protein ratio, Journal of Immunological Methods 167(1-2) (1994) 121-127.
[46] M.S. Hoque, S. Benjakul, T. Prodpran, Effect of heat treatment of film-forming solution on the properties of film from cuttlefish (Sepia pharaonis) skin gelatin, Journal of Food Engineering 96(1) (2010) 66-73.
[47] A. Chetouani, M. Elkolli, M. Bounekhel, D. Benachour, Synthesis and properties of novel hydrogels from oxidized pectin crosslinked gelatin for biomedical applications, Polymer Bulletin 71 (2014) 2303-2316.
[48] G. Xu, N. Xu, T. Ren, C. Chen, J. Li, L. Ding, Y. Chen, G. Chen, Z. Li, Y. Yu, Multifunctional chitosan/silver/tannic acid cryogels for hemostasis and wound healing, International Journal of Biological Macromolecules 208 (2022) 760-771.
[49] G.F. Alves-Silva, V.P. Romani, V.G. Martins, Different crosslinking as a strategy to improve films produced from external mesocarp of pequi (Caryocar brasiliense), Food Chemistry 432 (2024) 137202.
[50] C.S. Ki, D.H. Baek, K.D. Gang, K.H. Lee, I.C. Um, Y.H. Park, Characterization of gelatin nanofiber prepared from gelatin–formic acid solution, Polymer 46(14) (2005) 5094-5102.
[51] R. Mishra, A. Majeed, A. Banthia, Development and characterization of pectin/gelatin hydrogel membranes for wound dressing, International Journal of Plastics Technology 15 (2011) 82-95.
[52] A. Bigi, S. Panzavolta, K. Rubini, Relationship between triple-helix content and mechanical properties of gelatin films, Biomaterials 25(25) (2004) 5675-5680.
[53] C. Peña, K. De La Caba, A. Eceiza, R. Ruseckaite, I. Mondragon, Enhancing water repellence and mechanical properties of gelatin films by tannin addition, Bioresource technology 101(17) (2010) 6836-6842.
[54] N.-T. Nguyen, J.-H. Liu, A green method for in situ synthesis of poly (vinyl alcohol)/chitosan hydrogel thin films with entrapped silver nanoparticles, Journal of the Taiwan Institute of Chemical Engineers 45(5) (2014) 2827-2833.
[55] H. Fan, L. Wang, X. Feng, Y. Bu, D. Wu, Z. Jin, Supramolecular hydrogel formation based on tannic acid, Macromolecules 50(2) (2017) 666-676.
[56] M.S. Saharudin, R. Atif, I. Shyha, F. Inam, The degradation of mechanical properties in polymer nano-composites exposed to liquid media–a review, RSC advances 6(2) (2016) 1076-1089.
[57] D. Queen, J. Gaylor, J. Evans, J. Courtney, W. Reid, The preclinical evaluation of the water vapour transmission rate through burn wound dressings, Biomaterials 8(5) (1987) 367-371.
[58] Y.D. Boakye, C. Agyare, A. Hensel, Anti-infective properties and time-kill kinetics of Phyllanthus muellerianus and its major constituent, geraniin, (2016).
[59] K.-T. Chung, Z. Lu, M. Chou, Mechanism of inhibition of tannic acid and related compounds on the growth of intestinal bacteria, Food and Chemical Toxicology 36(12) (1998) 1053-1060.
[60] A.R. Shahverdi, A. Fakhimi, H.R. Shahverdi, S. Minaian, Synthesis and effect of silver nanoparticles on the antibacterial activity of different antibiotics against Staphylococcus aureus and Escherichia coli, Nanomedicine: Nanotechnology, Biology and Medicine 3(2) (2007) 168-171.

[61] J.R. Morones, J.L. Elechiguerra, A. Camacho, K. Holt, J.B. Kouri, J.T. Ramírez, M.J. Yacaman, The bactericidal effect of silver nanoparticles, Nanotechnology 16(10) (2005) 2346.
[62] Y. Yu, R. Cui, X. Wang, H. Yang, H. Li, Preparation of multifunctional poly (l-lactic acid) film using heparin-mimetic polysaccharide multilayers: Hemocompatibility, cytotoxicity, antibacterial and drug loading/releasing properties, International journal of biological macromolecules 155 (2020) 14-26.
[63] Y. Chen, Y. Zhang, F. Wang, W. Meng, X. Yang, P. Li, J. Jiang, H. Tan, Y. Zheng, Preparation of porous carboxymethyl chitosan grafted poly (acrylic acid) superabsorbent by solvent precipitation and its application as a hemostatic wound dressing, Materials Science and Engineering: C 63 (2016) 18-29.
[64] L.K. Meena, P. Raval, D. Kedaria, R. Vasita, Study of locust bean gum reinforced cyst-chitosan and oxidized dextran based semi-IPN cryogel dressing for hemostatic application, Bioactive Materials 3(3) (2018) 370-384.
[65] J. Wen, M. Weinhart, B. Lai, J. Kizhakkedathu, D.E. Brooks, Reversible hemostatic properties of sulfabetaine/quaternary ammonium modified hyperbranched polyglycerol, Biomaterials 86 (2016) 42-55.
[66] L. Wang, C. Hu, L. Shao, The antimicrobial activity of nanoparticles: present situation and prospects for the future, International journal of nanomedicine (2017) 1227-1249.
[67] A. Hebeish, M. El-Rafie, M.A. El-Sheikh, A.A. Seleem, M.E. El-Naggar, Antimicrobial wound dressing and anti-inflammatory efficacy of silver nanoparticles, International journal of biological macromolecules 65 (2014) 509-515.
[68] N. Lubick, Nanosilver toxicity: ions, nanoparticles， or both?, ACS Publications, 2008.
[69] G.A. Sotiriou, S.E. Pratsinis, Antibacterial activity of nanosilver ions and particles, Environmental science & technology 44(14) (2010) 5649-5654.
[70] C. Rigo, M. Roman, I. Munivrana, V. Vindigni, B. Azzena, C. Barbante, W.R. Cairns, Characterization and evaluation of silver release from four different dressings used in burns care, Burns 38(8) (2012) 1131-1142.
[71] F.M. Silva, R.J. Pinto, A.L. Daniel-da-Silva, T. Trindade, Cationic release behaviour of antimicrobial cellulose/silver nanocomposites, Cellulose 21 (2014) 3551-3560.
[72] A. Shahravan, T. Matsoukas, Encapsulation and controlled release from core–shell nanoparticles fabricated by plasma polymerization, Journal of Nanoparticle Research 14 (2012) 1-11.
[73] K. Kishore, S. Rajesh, S. Sivadas, N. Selvasudha, R. Barathidasan, H.R. Vasanthi, Pectin encapsulated novel nanocomposite augments wound healing in Sprague Dawley rats, Carbohydrate Polymer Technologies and Applications 6 (2023) 100370.
[74] J. Reinke, H. Sorg, Wound repair and regeneration, European surgical research 49(1) (2012) 35-43.
[75] N.P. Birch, L.E. Barney, E. Pandres, S.R. Peyton, J.D. Schiffman, Thermal-responsive behavior of a cell compatible chitosan/pectin hydrogel, Biomacromolecules 16(6) (2015) 1837-1843.
[76] M. Tummalapalli, M. Berthet, B. Verrier, B. Deopura, M. Alam, B. Gupta, Drug loaded composite oxidized pectin and gelatin networks for accelerated wound healing, International journal of pharmaceutics 505(1-2) (2016) 234-245.